

1       **Time-lapse monitoring of seismic velocity associated**  
2       **with 2011 Shinmoe-dake eruption using seismic**  
3       **interferometry**

4       **Kiwamu Nishida<sup>1</sup>, Yuta Mizutani<sup>1,2</sup>, Mie Ichihara<sup>1</sup>, Yosuke Aoki<sup>1</sup>**

5       <sup>1</sup>Earthquake Research Institute, University of Tokyo, 1-1-1 Yayoi 1, Bunkyo-ku, Tokyo 113-0032, Japan

6       <sup>2</sup>JX Nippon Oil & Gas Exploration Corp.

7       **Key Points:**

- 8       • A new technique of extended Kalman filtering for estimating the temporal change  
9       of seismic velocity is developed.
- 10      • Mass variations in the subsurface due to precipitation can explain observed sea-  
11      sonal variations in seismic velocity.
- 12      • Spatial and temporal variations in seismic velocity suggest that damage due to  
13      magma migration could be the origin.

---

Corresponding author: Kiwamu Nishida, [knishida@eri.u-tokyo.ac.jp](mailto:knishida@eri.u-tokyo.ac.jp)

**Abstract**

Seismic interferometry is a powerful tool to monitor the seismic velocity change associated with volcanic eruptions. For the monitoring, changes in seismic velocity with environmental origins (such as precipitation) are problematic. In order to model the environmental effects, we propose a new technique based on a state-space model. An extended Kalman filter estimates seismic velocity changes as state variables, with a first-order approximation of the stretching method. We apply this technique to three-component seismic records in order to detect the seismic velocity change associated with the Shinmoe-dake eruptions in 2011 and 2018. First, ambient noise cross-correlations were calculated from May 2010 to April 2018. We also modeled seismic velocity changes resulting from precipitation and the 2016 Kumamoto earthquake, with exponential type responses. Most of the results show no significant changes associated with the eruptions, although gradual inflation of the magma reservoir preceded the 2011 eruption by one year. The observed low sensitivity to static stress changes suggests that the fraction of geofluid and crack density at about 1 km depth is small, and the shapes could be circular. Only one station pair west of the crater shows the significant drop associated with the eruption in 2011. The gradual drop of seismic velocity up to 0.05% preceded the eruption by one month. When the gradual drop began, volcanic tremors were activated at about 2 km depth. These observations suggest that the drop could be caused by damage accumulation due to vertical magma migration beneath the summit.

**1 Introduction**

Shinmoe-dake forms part of a group of Kirishima volcanoes, located in Kyusyu Japan, and is an active volcano. Over a period of ten years, it experienced a major eruption in 2011, and an effusive eruption in 2018. In 2011, the eruptive sequence started with sub-Plinian eruptions (January 26-27th), followed by a lava effusion (January 28-31st), and culminating in Vulcanian eruptions (1-10 Feb.) (Nakada et al., 2013). Observations from Global Navigation Satellite Systems (GNSS) show that the gradual inflation of the magma reservoir preceded the 2011 eruption by one year. The magma reservoir is located approximately 7 km northwest of Shinmoe-dake at a depth of approximately 8 km below sea level (BSL) (Nakao et al., 2013; Kozono et al., 2013). When the inflation started, low-frequency earthquakes (LFE) at a depth of 20-27 km was activated, suggesting the migration of magma from a deeper region (Kurihara et al., 2019). During the 2011 erup-

46 tions, the GNSS data indicate the co-eruption deflation of the magma reservoir. Tilt ob-  
47 servation showed that an-hour-long inflation and rapid deflation at a shallow depth (around  
48 500 m) near the summit right before the first sub-Plinian event (Takeo et al., 2013). Also  
49 stepwise local tilt inflations were reported twice in about a week before the sub-Plinian  
50 event (Ichihara & Matsumoto, 2017). During the eruption, explosion earthquakes were  
51 observed (Nakamichi et al., 2013). The activities suggest that the magma touched an  
52 aquifer at shallow depths of about -1.0 km BSL (e.g., Kagiya et al., 1996). Before and  
53 during the sub-Plinian eruptions, migration of gas (probably with magma) also activated  
54 continuous volcanic tremors (Ichihara & Matsumoto, 2017). These were located beneath  
55 the crater for one week before the major eruption, and they rose from a depth of a few  
56 kilometers to the near-surface aquifer three times. The heat transported to the water  
57 layer could trigger the sub-Plinian eruptions (Ichihara & Matsumoto, 2017). In order  
58 to understand the magma plumping system, pertinent information from depths of 1 to  
59 10 km is crucial. However, we cannot detect earthquake activity at these depths before  
60 the major eruptions associated with the magma migration (Ueda et al., 2013) and other  
61 geophysical phenomena.

62 Seismic interferometry is a powerful technique for monitoring seismic velocity in  
63 the depth range of interest. In recent years, the number of applications of seismic inter-  
64 ferometry has increased. In the analysis, the cross-correlation function between ambi-  
65 ent noise records of a pair of stations can be regarded as a virtual seismic waveform, recorded  
66 at one station when the source is placed at the other station. In any time period, the  
67 seismic velocity around the station pair can be estimated from the cross-correlation func-  
68 tion calculated without an earthquake; thus, seismic interferometry has been applied in  
69 many studies to monitor temporal changes in seismic velocity (e.g., Obermann & Hillers,  
70 2019). This technique has been applied for detecting seismic wave velocity changes af-  
71 ter large earthquakes (e.g., Wegler & Sens-Schönfelder, 2007; Wegler et al., 2009; Bren-  
72 guier, Campillo, et al., 2008; Brenguier et al., 2014), those of a slow slip event (Rivet et  
73 al., 2011), and those associated with volcanic eruptions: e.g., the Piton de La Fournaise  
74 volcano, La Réunion, France (Brenguier, Shapiro, et al., 2008), Mt. Asama, Japan (Nagaoka  
75 et al., 2010), Merapi volcano, Indonesia (Budi-Santoso & Lesage, 2016), Ubinas volcano,  
76 Peru (Machacca et al., 2019) and Kilauea volcano, USA (Donaldson et al., 2017). For  
77 example, Brenguier, Shapiro, et al. (2008) detected a drop in seismic velocity of the or-  
78 der of 0.1% for a number of days preceding the eruption of the Piton de La Fournaise

79 volcano, and the velocity recovered at a time scale of about 10-20 days. There are two  
80 potential sources for the temporal changes (Olivier et al., 2019). The first is pressuriza-  
81 tion due to the magma migration in a linear elastic regime. In this regime, stress sen-  
82 sitivity of seismic velocity change is a proxy for inferring the state of the material: in par-  
83 ticular the existence of geofluid (Brenguier et al., 2014). The second source is damage  
84 accumulation beyond the linear elastic regime.

85 The biggest technical difficulty in monitoring is the separation of temporal vari-  
86 ations of volcanic origin from environmental variations. Many researchers reported sea-  
87 sonal variations associated with environmental phenomena: rainfall (e.g., Rivet et al.,  
88 2015), air pressure (e.g., Niu et al., 2008), and thermo-elasticity (e.g., Hillers et al., 2015).  
89 In the region of Mt. Shimoe-dake, daily precipitation exceeds 100 mm for several days  
90 in a year, while the annual precipitation is more than 4000 mm. Wang et al. (2017) re-  
91 ported that rainfall is the major source of the observed temporal changes in this area  
92 (Kyusyu). The Merapi Volcano, Indonesia, Sens-Schönfelder and Wegler (2006) also ex-  
93 perience the observed dominance of seasonal variations. Temporal changes in ground-  
94 water levels based on precipitation data can explain the observed strong seasonal vari-  
95 ations in both cases. Such strong seasonal variations have the potential to mask a tem-  
96 poral change associated with volcanic activities; thus, correction for rainfall is crucial for  
97 inferring the temporal changes associated with volcanic activity (Rivet et al., 2015; Wang  
98 et al., 2017).

99 Earthquakes also contaminate temporal changes in seismic velocities associated with  
100 volcanic activities. In particular, this region experienced the 2016 Kumamoto earthquake  
101 of Mw 7.3 (e.g., Kato et al., 2016). The seismic-velocity dropped during the earthquake,  
102 and recovered over a time scale of several months (Nimiya et al., 2017). Since the seismic-  
103 velocity reduction on the order of 0.1% could be comparable to typical temporal vari-  
104 ations associated with volcanic activities, it should be subtracted. Moreover, the suscep-  
105 tibility, which is defined by the ratio between observed reductions in seismic velocity and  
106 the estimated dynamic stress (Brenguier et al., 2014), is a good proxy for discussing the  
107 state of geofluid in the upper crust associated with a volcanic process.

108 For the separation of seasonal, earthquake's and volcanic origins, we propose a new  
109 technique based on a state-space model. We show that an extended Kalman filter is fea-

110 sible for estimation in section 4. The magma migration based on the observed tempo-  
 111 ral changes is then discussed.

## 112 **2 Cross-correlation analysis**

113 We used three component seismograms recorded at eight stations (six broadband  
 114 sensors and two short-period sensors with a natural frequency of 1 Hz) from May 1st,  
 115 2010 to April 30th, 2018, shown in Figure 1. Five stations were deployed by the Earth-  
 116 quake Research Institute, the University of Tokyo, and the other three were deployed  
 117 by the National Research Institute for Earth Science and Disaster Prevention (NIED).  
 118 The details of the sensors are shown in Table 1. We used daily precipitation data recorded  
 119 by a station (Ebino shown by the white circle in Figure 1) of the Japan Meteorological  
 120 Agency (JMA) for correcting the precipitation effects as described in section 5.1.

121 First, the data were down-sampled from 100 Hz to 2.5 Hz. The instrumental re-  
 122 sponses were corrected in time domain (Maeda et al., 2011) according to the sensor type,  
 123 and all records were bandpass-filtered from 0.15 to 0.90 Hz. For each station pair, the  
 124 two horizontal components were rotated into radial and transverse coordinates accord-  
 125 ing to the geometry of the station pair: the radial direction is parallel to the great cir-  
 126 cle path between the station pair, and the transverse direction is perpendicular to the  
 127 great circle path (Nishida et al., 2008). The daily records were divided into segments of  
 128 409.6 s, with an overlap of 204.8 s.

129 To reject noisy data, which include transient phenomena such as high instrumen-  
 130 tal noise or earthquakes, we discarded the noisy segments as follows. For one-day data  
 131 of each component at a station, we estimated the root mean squared amplitudes (RMSs)  
 132 of all the segments. For each component of one-day data, we defined the threshold to  
 133 be twice the median value of RMSs for all the segments in one day. If the RMS of a seg-  
 134 ment was larger than the threshold, the segment was discarded.

135 We then took cross-correlation functions (CCFs) of all possible pairs of stations,  
 136 and all possible component combinations for each station pair. We stacked the CCFs of  
 137 the selected segments over one day with the spectral whitening, as done in previous stud-  
 138 ies (Bensen et al., 2007). The daily CCFs of the individual pairs of stations were rep-  
 139 resented by  $\phi_t^p(\tau)$ , where  $\tau$  shows lag time, and the subscript  $t$  is an integer, which rep-  
 140 represents days (JST), and the superscript  $p$  shows the pair of components (9 components:

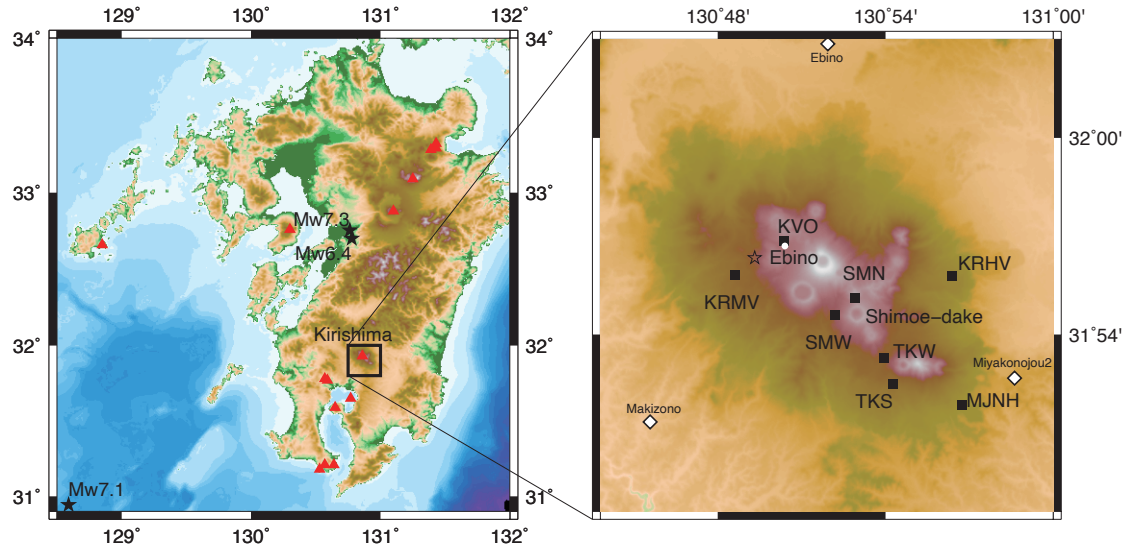


**Figure 1.** Left: Red triangles show active volcanoes. Black stars represent the hypocenters of earthquakes: (i) Mw 6.4, April 14th (UTC), 2016, the foreshock of the Kumamoto earthquake, (ii) Mw 7.3, April 15th (UTC), 2016, the mainshock of the Kumamoto earthquake and (ii) Mw 7.1, November 13th (UTC), 2015, the Satsuma earthquake. Right: Station distribution. Black squares show station locations, and the white circle shows the JMA weather station. Three white diamond symbols show the locations of GEONET stations operated by the Geospatial Information Authority of Japan. The star symbol shows the location of volumetric source at a depth of 8.35 km (Nakao et al., 2013). The topography in the right panel is given by the corresponding Shuttle Radar Topography Mission (Farr et al., 2007).

Network	Station name	Sensor type
ERI	KVO	L4-C (1 s, -2/2/2011), Trillium-120 (120 s, 2/3/2011-)
ERI	SMN	Trillium-40 (40 s, -7/22/2010) Trillium-120 (120 s, 7/23/2010-)
ERI	SMW	L4-C (1 s)
ERI	TKW	CMG3T (100 s)
ERI	TKS	Trillium-40 (40 s, -2/4/2011) Trillium-120 (120 s, 2/5/2011-)
NIED (V-net)	KRHV	Trillium-240 (240 s)
NIED (V-net)	KRMV	Trillium-240 (240 s)
NIED (Hi-net)	MJNH	Hi-net 1 Hz velocity meter (1 s)

**Table 1.** Sensor type for each station. ERI represents a station deployed by the Volcano Research Center, Earthquake Research Institute, the University of Tokyo. NIED (V-net) means a station of the Volcano Observation network deployed by the National Research Institute for Earth Science and Disaster Prevention, and NIED (Hi-net) means a station of High-Sensitivity Seismograph Network deployed by NIED.

141  $R - R$ ,  $R - T$ ,  $\dots$ ,  $Z - Z$ , where  $R$  is the radial component, and  $T$  is transverse com-  
142 ponent, and  $Z$  is vertical component). Figure 2 shows a typical example of daily CCFs,  
143 which are stable even in their coda parts for eight years. Figure 3 shows a typical ex-  
144 ample of the mean power spectrum of the mean CCF between a pair of broadband sta-  
145 tions, which shows dominance in lower frequencies from 0.25-0.5 Hz, even after the spec-  
146 tral whitening.

### 147 **3 Measurements of seismic velocity change**

148 Seismic interferometry is feasible for monitoring seismic wave velocity between pairs  
149 of stations. The principle of seismic interferometry is that the CCF between a station  
150 pair represents the seismic wavefield as though a source lies at one station and a receiver  
151 lies at the other. However, disadvantage of this technique is that the measurements are  
152 overly sensitive to source heterogeneity (e.g., Weaver et al., 2009). This causes a trade-  
153 off between a temporal change of seismic velocity and that of source heterogeneity. Al-  
154 though the direct waves are sensitive to the source heterogeneity, the coda part becomes  
155 insensitive with increasing lapse time. This is because the seismic wavefield loses the source

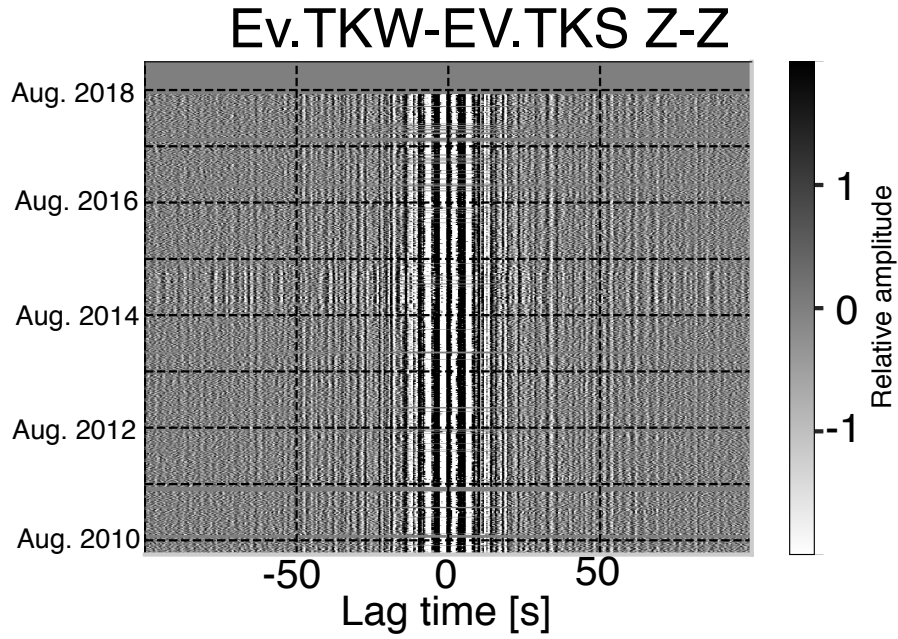


**Figure 2.** Daily CCFs of Z-Z component (0.2-0.4 Hz) between TKS and TKW. The vertical axis shows date, the horizontal axis shows lag time.

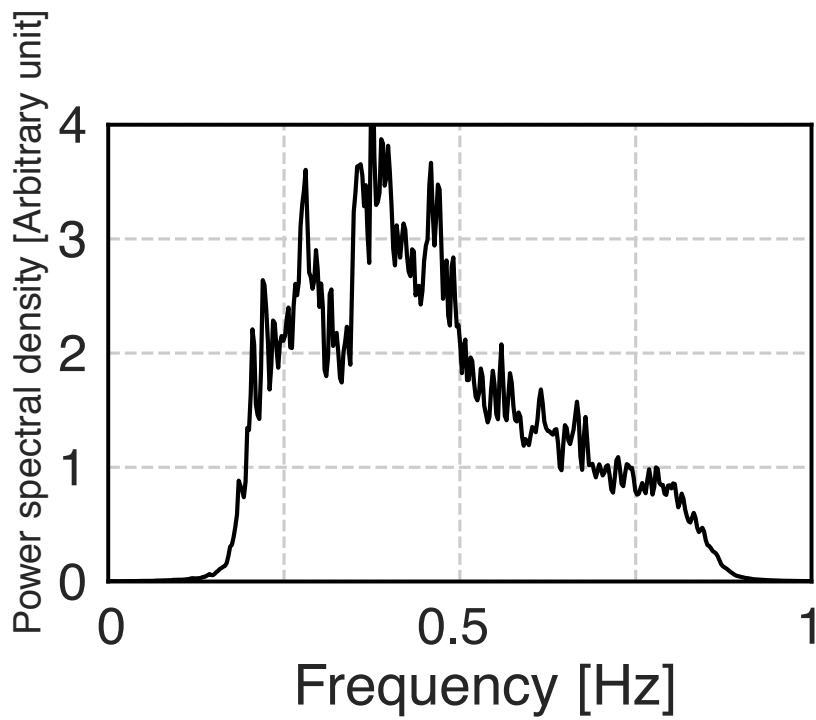


**Figure 3.** Power spectrum averaged over all CCFs between TKS and TKW with the time window from -99.6 to -20 s and from 20 to 99.6 s.

156 information over multiple scatterings (Colombi et al., 2014). If the seismic velocity changes  
 157 uniformly in space, the arrival time delays with lapse time. This approach is known as  
 158 the doublet method in frequency domain, first applied to earthquake coda (Poupinet et  
 159 al., 1984). This method is also feasible for monitoring of seismic velocity with seismic  
 160 interferometry (e.g., Brenguier et al., 2014). We used the method in the time domain,  
 161 known as the stretching method (Weaver & Lobkis, 2000), because the linearization is  
 162 easier for an application of an extended Kalman filter as described in the next section.

163 We constructed a model function,  $m^p(A_t, \gamma_t; \tau)$ , for the observed CCF  $\phi_t^p(\tau)$  by stretch-  
 164 ing the reference CCF  $\varphi_{ref}^p(\tau)$  as,

$$165 \quad m^p(A_t, \gamma_t; \tau) = A_t \varphi_{ref}^p(\tau(1 + \gamma_t)), \quad (1)$$

166 where  $\gamma_t$  is the stretching factor,  $A_t$  is amplitude and the subscript  $t$  represents day. The  
 167 reference CCF  $\varphi_{ref}^p(\tau)$  was estimated by averaging all the observed CCFs  $\phi_t^p(\tau)$  over days  
 168  $t$ .

169 To estimate the temporal evolution of  $\gamma_t$ , Weaver and Lobkis (2000) constructed  
 170 a dilation correlation coefficient between waveforms  $X^p$  as,

$$171 \quad X^p(\gamma_t) = \frac{\int \phi_t^p(\tau) m^p(A_t, \gamma_t; \tau) d\tau}{\sqrt{\int \phi_t^p(\tau)^2 d\tau} \sqrt{\int (m^p(A_t, \gamma_t; \tau))^2 d\tau}}. \quad (2)$$

172 By maximizing the correlation, the temporal variation  $\gamma_t$  can be estimated. Several re-  
 173 searchers have used this method to measure the temporal changes in seismic velocity.  
 174 To enhance the signal to noise ratio, measurements over many station pairs and com-  
 175 ponents were averaged. Bayesian approaches (Tarantola & Valette, 1982) for these mea-  
 176 surements are feasible for more reliable estimations (Brenguier et al., 2016).

177 To enhance the flexibility of the Bayesian approach, we developed a new method  
 178 of an extended Kalman filter based on the state-space model (e.g., Segall & Matthews,  
 179 1997; Durbin & Koopman, 2012). This method, successively, minimizes the squared dif-  
 180 ference given by

$$181 \quad S(A_t, \gamma_t) \equiv \int (\phi_t^p(\tau) - m^p(A_t, \gamma_t; \tau))^2 d\tau. \quad (3)$$

182  $A_t$  and  $\gamma_t$  are recognized as state variables for the state modeling as shown in the next  
 183 section.

184 **4 State Space modeling**

185 Here we considered state variables  $\boldsymbol{\alpha}_t$ , which describe the amplitude  $A_t$  and the  
 186 stretching factor  $\gamma_t$  at  $t = 1, \dots, n$  assuming that the state variables are common to  
 187 all the 9 components for each station pair. The state variables and the data vector of  
 188 observed CCF  $\mathbf{y}_t^p$  for a  $p$ th component are defined by

$$189 \quad \boldsymbol{\alpha}_t \equiv \begin{pmatrix} A_t \\ \gamma_t \end{pmatrix}, \mathbf{y}_t^p \equiv \begin{pmatrix} \phi_t^p(-\tau_e) \\ \vdots \\ \phi_t^p(-\tau_s) \\ \phi_t^p(\tau_s) \\ \vdots \\ \phi_t^p(\tau_e) \end{pmatrix}, \quad (4)$$

190 where  $\tau_s$  is the start of lag time (20 s) and  $\tau_e$  is the end of lag time (99.6 s). They obeyed  
 191 the following relations:

$$192 \quad \mathbf{y}_t^p = \mathbf{m}^p(\boldsymbol{\alpha}_t + \mathbf{R}_t + \mathbf{E}_t) + \boldsymbol{\epsilon}_t, \quad \boldsymbol{\epsilon}_t \sim \mathcal{N}(0, \mathbf{H}_t) \quad (5)$$

$$193 \quad \boldsymbol{\alpha}_{t+1} = \boldsymbol{\alpha}_t + \boldsymbol{\eta}_t, \quad \boldsymbol{\eta}_t \sim \mathcal{N}(0, \mathbf{Q}_t), \quad (6)$$

194

195 where  $\mathbf{R}_t$  is an explanatory variable related to precipitation and  $\mathbf{E}_t$  is an explanatory  
 196 variable associated with the seismic-velocity drop during the 2016 Kumamoto earthquake,  
 197 respectively.  $\boldsymbol{\epsilon}_t$  and  $\boldsymbol{\eta}_t$  are mutually independent random variables, subject to normal  
 198 distribution ( $\mathcal{N}$ ) with zero means and covariance matrix  $\mathbf{H}_t$  and  $\mathbf{Q}_t$ , respectively. The  
 199 model  $\mathbf{m}^p$  are defined by

$$200 \quad \mathbf{m}^p(\boldsymbol{\alpha}_t + \mathbf{R}_t + \mathbf{E}_t) \equiv \begin{pmatrix} m^p(\boldsymbol{\alpha}_t + \mathbf{R}_t + \mathbf{E}_t; -\tau_e) \\ \vdots \\ m^p(\boldsymbol{\alpha}_t + \mathbf{R}_t + \mathbf{E}_t; -\tau_s) \\ m^p(\boldsymbol{\alpha}_t + \mathbf{R}_t + \mathbf{E}_t; \tau_s) \\ \vdots \\ m^p(\boldsymbol{\alpha}_t + \mathbf{R}_t + \mathbf{E}_t; \tau_e) \end{pmatrix}. \quad (7)$$

201 Since the sampling interval of CCFs is 0.4 s, the dimension of the vectors  $\mathbf{y}_t^p$  and  $\mathbf{m}^p$  is  
 202  $2 \cdot ((\tau_e - \tau_s)/0.4 + 1) = 400$ . With an assumption of the time invariance of data covari-  
 203 ance with respect to time and lag time,  $\mathbf{H}_t$  can be written by a diagonal matrix:

$$204 \quad \mathbf{H}_t \equiv h_0 \mathbf{I}, \quad (8)$$

205 where  $h_0$  is a prior data covariance and  $\mathbf{I}$  is the  $400 \times 400$  identity matrix. Assuming  
 206 that the amplitude  $A_t$  does not correlate the seismic velocity change  $\gamma_t$ , we can write  $\mathbf{Q}_t$   
 207 as a diagonal matrix:

$$208 \quad \mathbf{Q}_t \equiv \begin{pmatrix} q_0 & 0 \\ 0 & q_1 \end{pmatrix}, \quad (9)$$

209 where  $q_0$  and  $q_1$  are a prior model covariance.  $h_0$  is estimated from the time average of  
 210 the squared difference between  $\phi_t^p(\tau)$  and the reference  $\varphi_{ref}^p(\tau)$ . Since the amplitude  $A_t$   
 211 is a kind of normalization factor, it is difficult to separate the origins: volcanic, precipi-  
 212 tation, or earthquake. For simplicity, we omitted the amplitude term  $A_t$  for precipita-  
 213 tion and earthquakes. Accordingly  $\mathbf{R}_t$  and  $\mathbf{E}_t$  are given by,

$$214 \quad \mathbf{R}_t \equiv \begin{pmatrix} 0 \\ r_t \end{pmatrix}, \mathbf{E}_t \equiv \begin{pmatrix} 0 \\ e_t \end{pmatrix}. \quad (10)$$

215 The the state variable  $\boldsymbol{\alpha}_t$  has an initial value  $\mathbf{a}_1$  at  $t = 1$  subject to a normal dis-  
 216 tribution  $\sim N(\mathbf{a}_1, \mathbf{P}_1)$  defined by

$$217 \quad \mathbf{a}_1 \equiv \begin{pmatrix} A_1 \\ \gamma_1 \end{pmatrix}, \mathbf{P}_1 \equiv \begin{pmatrix} p_0 & 0 \\ 0 & p_1 \end{pmatrix}, \quad (11)$$

218 where  $A_1$  is a prior initial amplitude,  $\gamma_1$  is a prior initial stretching factor,  $p_0$  and  $p_1$  are  
 219 a prior model cocariance for the initial value.

220 First, we assumed that  $\mathbf{Q}_t$ ,  $\mathbf{R}_t$ ,  $\mathbf{E}_t$  and  $\mathbf{P}_1$  are given in advance; that is, they are  
 221 recognized as hyper-parameters. In the next step, we estimated the hyper-parameters  
 222 using the Maximum Likelihood Method as discussed in the next section.

223 We linearized the equation (1) (e.g., Weaver et al., 2011) in order to apply the ex-  
 224 tended Kalman filter. We consider the update of state variable from the initial guess  $\hat{\boldsymbol{\alpha}}_t \equiv$   
 225  $(\hat{A}_t, \hat{\gamma}_t)^T$ . Assume that the increment from the initial guess  $\Delta\boldsymbol{\alpha}$  is small, Taylor series  
 226 of  $\mathbf{m}^p$  in equation (5) at around the initial guess  $\hat{\boldsymbol{\alpha}}_t$  up to 1st order lead the following  
 227 equation,

$$228 \quad \mathbf{m}^p(\hat{\boldsymbol{\alpha}}_t + \Delta\boldsymbol{\alpha} + \mathbf{R}_t + \mathbf{E}_t) = \mathbf{m}^p(\hat{\boldsymbol{\alpha}}_t + \mathbf{R}_t + \mathbf{E}_t) + \boldsymbol{\zeta}_t^p \Delta\boldsymbol{\alpha}, \quad (12)$$

229 where

$$230 \quad \zeta_t^p = \begin{pmatrix} \varphi_{ref}^p(-(1 + \hat{\gamma}_t + r_t + e_t)\tau_e) & -\hat{A}_t\tau_e\dot{\varphi}_{ref}^p(-(1 + \hat{\gamma}_t + r_t + e_t)\tau_e) \\ \vdots & \vdots \\ \varphi_{ref}^p(-(1 + \hat{\gamma}_t + r_t + e_t)\tau_s) & -\hat{A}_t\tau_s\dot{\varphi}_{ref}^p(-(1 + \hat{\gamma}_t + r_t + e_t)\tau_s) \\ \varphi_{ref}^p((1 + \hat{\gamma}_t + r_t + e_t)\tau_s) & \hat{A}_t\tau_s\dot{\varphi}_{ref}^p((1 + \hat{\gamma}_t + r_t + e_t)\tau_s) \\ \vdots & \vdots \\ \varphi_{ref}^p((1 + \hat{\gamma}_t + r_t + e_t)\tau_e) & \hat{A}_t\tau_e\dot{\varphi}_{ref}^p((1 + \hat{\gamma}_t + r_t + e_t)\tau_e) \end{pmatrix}, \quad (13)$$

231 and  $\dot{\varphi}$  represents the derivative of  $\varphi$ .

232 Since nine components of the cross-correlation functions were used in this study,  
233 we define the following vectors:

$$234 \quad \mathbf{Y}_t \equiv \begin{pmatrix} \mathbf{y}_t^{RR} \\ \mathbf{y}_t^{RT} \\ \mathbf{y}_t^{RZ} \\ \mathbf{y}_t^{TR} \\ \mathbf{y}_t^{TT} \\ \mathbf{y}_t^{TZ} \\ \mathbf{y}_t^{ZR} \\ \mathbf{y}_t^{ZT} \\ \mathbf{y}_t^{ZZ} \end{pmatrix}, \quad \mathbf{Z}_t(\hat{\alpha}_t) \equiv \begin{pmatrix} \zeta_t^{RR} \\ \zeta_t^{RT} \\ \zeta_t^{RZ} \\ \zeta_t^{TR} \\ \zeta_t^{TT} \\ \zeta_t^{TZ} \\ \zeta_t^{ZR} \\ \zeta_t^{ZT} \\ \zeta_t^{ZZ} \end{pmatrix}, \quad \mathbf{M}_t(\hat{\alpha}_t) \equiv \begin{pmatrix} \mathbf{m}^{RR}(\hat{\alpha}_t + \mathbf{R}_t + \mathbf{E}_t) \\ \mathbf{m}^{RT}(\hat{\alpha}_t + \mathbf{R}_t + \mathbf{E}_t) \\ \mathbf{m}^{RZ}(\hat{\alpha}_t + \mathbf{R}_t + \mathbf{E}_t) \\ \mathbf{m}^{TR}(\hat{\alpha}_t + \mathbf{R}_t + \mathbf{E}_t) \\ \mathbf{m}^{TT}(\hat{\alpha}_t + \mathbf{R}_t + \mathbf{E}_t) \\ \mathbf{m}^{TZ}(\hat{\alpha}_t + \mathbf{R}_t + \mathbf{E}_t) \\ \mathbf{m}^{ZR}(\hat{\alpha}_t + \mathbf{R}_t + \mathbf{E}_t) \\ \mathbf{m}^{ZT}(\hat{\alpha}_t + \mathbf{R}_t + \mathbf{E}_t) \\ \mathbf{m}^{ZZ}(\hat{\alpha}_t + \mathbf{R}_t + \mathbf{E}_t) \end{pmatrix} \quad (14)$$

#### 235 4.1 Calculation of the reference CCF

236 First, we estimated the reference CCF  $\varphi_{ref}^p$  for the  $p$ th component pair as,

$$237 \quad \varphi_{ref}^p(\tau) = \frac{1}{n} \sum_{t=1}^n \phi_t^p(\tau). \quad (15)$$

238 With the preliminary reference CCF, preliminary  $\hat{\gamma}_t$  was measured using an extended  
239 Kalman filter and smoother described in the following subsection. Then we recalculated  
240 the reference as

$$241 \quad \varphi_{ref}^p(\tau) = \frac{1}{n} \sum_{t=1}^n \phi_t^p(\tau(1 + \hat{\gamma}_t)). \quad (16)$$

242 After recalculating  $\hat{\gamma}_t$  with the revised reference, we measured the temporal variations  
243 that are discussed herein.

## 244 4.2 Extended Kalman filter

245 The state vector  $\alpha_t$  was estimated by the recursive linear Kalman (forward) filter  
 246 and (backward) smoother. The Kalman filter/smoothing is a powerful solver of a state-  
 247 space model, which obeys Gaussian distribution (e.g., Durbin & Koopman, 2012). The  
 248 method has been applied for many geophysical problems (e.g. geodetic inversions, Segall  
 249 & Matthews, 1997; Aoki et al., 1999), and recursive travel-time inversion in seismology  
 250 (Ogiso et al., 2005). Since we assumed that state vectors obey a normal distribution, the  
 251 means and the covariance matrices characterized the statistics of the vector completely.  
 252 Let us consider the conditional mean and covariance matrix of the state variables at time  
 253  $t = 2 \cdots n$  for given data through  $\mathbf{Y}_1, \cdots, \mathbf{Y}_{t-1}$  as,

$$254 \hat{\alpha}_{t|t-1} \equiv E(\alpha_t | \mathbf{Y}_1, \cdots, \mathbf{Y}_{t-1}) \quad (17)$$

$$255 \hat{\mathbf{P}}_{t|t-1} \equiv Cov(\alpha_t | \mathbf{Y}_1, \cdots, \mathbf{Y}_{t-1}), \quad (18)$$

257 where  $n$  is number of the data,  $E()$  represents expectation, and  $Cov()$  represents covari-  
 258 ance.  $\hat{\alpha}_{t|t-1}$  is also known as the one-step ahead predictor (Durbin & Koopman, 2012).  
 259 Since no data can constrain  $\hat{\alpha}_{1|0}$  and  $\hat{\mathbf{P}}_{1|0}$ , they are given by the initial values:  $\hat{\alpha}_{1|0} =$   
 260  $\mathbf{a}_1$  and  $\hat{\mathbf{P}}_{1|0} = \mathbf{P}_1$ .

261 These are updated from the initial value  $\mathbf{a}_1$  and  $\mathbf{P}_1$  using the following equation:

$$262 \hat{\alpha}_{t+1|t} = \hat{\alpha}_{t|t-1} + \mathbf{K}_t \mathbf{v}_t \quad (19)$$

$$263 \hat{\mathbf{P}}_{t+1|t} = \hat{\mathbf{P}}_{t|t-1} - \mathbf{K}_t (\mathbf{Z}_t \hat{\mathbf{P}}_{t|t-1} \mathbf{Z}_t^T + \mathbf{H}_t) \mathbf{K}_t^T + \mathbf{Q}_t, \quad (20)$$

265 where Kalman gain  $\mathbf{K}_t$  is given by

$$266 \mathbf{K}_t = \hat{\mathbf{P}}_{t|t-1} \mathbf{Z}_t^T (\mathbf{H}_t + \mathbf{Z}_t \hat{\mathbf{P}}_{t|t-1} \mathbf{Z}_t^T)^{-1}, \quad (21)$$

267 and the innovation vector  $\mathbf{v}_t$  is given by

$$268 \mathbf{v}_t = \mathbf{Y}_t - \mathbf{M}_t(\hat{\alpha}_{t|t-1}). \quad (22)$$

269 Since the number of model parameters of 2 is much smaller than length of  $\mathbf{Y}_t$  of 36000  
 270 (9 components  $\times$  400 points), the matrix calculation of equation (21) can be reduced us-  
 271 ing the following matrix inversion lemma (Tarantola & Valette, 1982; Ogiso et al., 2005),

$$272 (\mathbf{H}_t + \mathbf{Z}_t \hat{\mathbf{P}}_{t|t-1} \mathbf{Z}_t^T)^{-1} = \mathbf{H}_t^{-1} - \mathbf{H}_t^{-1} \mathbf{Z}_t (\hat{\mathbf{P}}_{t|t-1}^{-1} + \mathbf{Z}_t^T \mathbf{H}_t^{-1} \mathbf{Z}_t)^{-1} \mathbf{Z}_t^T \mathbf{H}_t^{-1}. \quad (23)$$

273 Here we assumed that the errors of the CCF are independent of lag time, and the  
 274 variances were the same throughout the lag time. Since we assumed that the covariance

275 matrix of data error  $\mathbf{H}_t$  is represented by  $\mathbf{H}_t = h_0 \mathbf{I}$  (equation (8)), the forward recur-  
 276 sive equations (19) and (20) could be simplified as,

$$277 \quad \hat{\boldsymbol{\alpha}}_{t+1|t} = \hat{\boldsymbol{\alpha}}_{t|t-1} + \boldsymbol{\Xi}_t \boldsymbol{\Gamma}_t \quad (24)$$

$$278 \quad \hat{\mathbf{P}}_{t+1|t} = \hat{\mathbf{P}}_{t|t-1} - \boldsymbol{\Xi}_t (\mathbf{S}_t \hat{\mathbf{P}}_{t|t-1} \mathbf{S}_t + h_0 \mathbf{S}_t) \boldsymbol{\Xi}_t^T + \mathbf{Q}_t, \quad (25)$$

280 where  $\mathbf{S}_t$  and  $\boldsymbol{\Xi}_t$   $2 \times 2$  matrices as:

$$281 \quad \mathbf{S}_t \equiv \sum_p (\boldsymbol{\zeta}_t^p)^T \boldsymbol{\zeta}_t^p, \quad (26)$$

$$282 \quad \boldsymbol{\Gamma}_t \equiv \sum_p (\boldsymbol{\zeta}_t^p)^T \mathbf{v}_t^p, \quad (27)$$

$$283 \quad \boldsymbol{\Xi}_t \equiv \left( \frac{1}{h_0} \hat{\mathbf{P}}_{t|t-1} - \frac{1}{h_0^2} \hat{\mathbf{P}}_{t|t-1} \mathbf{S}_t \left( \frac{\mathbf{S}_t}{h_0} + \hat{\mathbf{P}}_{t|t-1}^{-1} \right)^{-1} \right). \quad (28)$$

### 285 4.3 Kalman smoother

286 Next, let us consider the conditional mean  $\hat{\boldsymbol{\alpha}}_{t|n}$  and conditional covariance matrix  
 287  $\hat{\mathbf{P}}_{t|n}$  of the state variables at time  $t$  for all data through  $\mathbf{Y}_1, \dots, \mathbf{Y}_n$ . With the  $\hat{\boldsymbol{\alpha}}_{t|t-1}$  and  
 288  $\hat{\mathbf{P}}_{t|t-1}$  ( $t = 2, \dots, n$ ) estimated in the previous subsection, they can be calculated by  
 289 the following backward recursive equations,

$$290 \quad \hat{\boldsymbol{\alpha}}_{t|n} = \hat{\boldsymbol{\alpha}}_{t|t-1} + \hat{\mathbf{A}}_t (\hat{\boldsymbol{\alpha}}_{t+1|n} - \hat{\boldsymbol{\alpha}}_{t|t-1}), \quad (29)$$

$$291 \quad \hat{\mathbf{P}}_{t|n} = \hat{\mathbf{P}}_{t+1|t} - \mathbf{Q}_t + \hat{\mathbf{A}}_t (\hat{\mathbf{P}}_{t+1|n} - \hat{\mathbf{P}}_{t+1|t}) \hat{\mathbf{A}}_t^T, \quad (30)$$

293 where  $\hat{\mathbf{A}}_t$  is defined by

$$294 \quad \hat{\mathbf{A}}_t = \left( \mathbf{I} - \mathbf{Q}_t \hat{\mathbf{P}}_{t+1|t}^{-1} \right), \quad (31)$$

295 The recursive equations were applied successively backward as  $t = n - 1, \dots, 1$ .

### 296 4.4 Temporal change of seismic wave velocity

297 First, we tentatively estimated the temporal variations without the explanatory vari-  
 298 ables. For given hyper-parameters  $r_t = e_t = 0$ ,  $p_0 = 5 \times 10^{-4}$ ,  $p_1 = 5 \times 10^{-5}$ , we esti-  
 299 mated the state variables using the extended Kalman filter and smoother. Figure 4 shows  
 300 the result of temporal variations in seismic velocity  $\hat{\gamma}_{t|n}$  and the corresponding standard  
 301 deviation by applying CCFs of the station pair between TKW and TKS. The figure shows  
 302 clear seasonal variation, and the velocity drops coincide with strong rainfalls (blue bars  
 303 in the figure). The red line shows the precipitation model (see the next section for de-  
 304 tails). This figure also shows a sudden velocity drop of about 0.1 % when the Kumamoto

305 earthquake occurred in 2016. To detect signals associated with volcanic eruptions, we  
 306 subtracted the precipitation effects and the earthquake drop from the temporal varia-  
 307 tions in seismic velocity. For the subtraction, we infer the hyper-parameters, which rep-  
 308 resent the model covariances, precipitation effects, and earthquake drop by the Maxi-  
 309 mum Likelihood method in the next section.

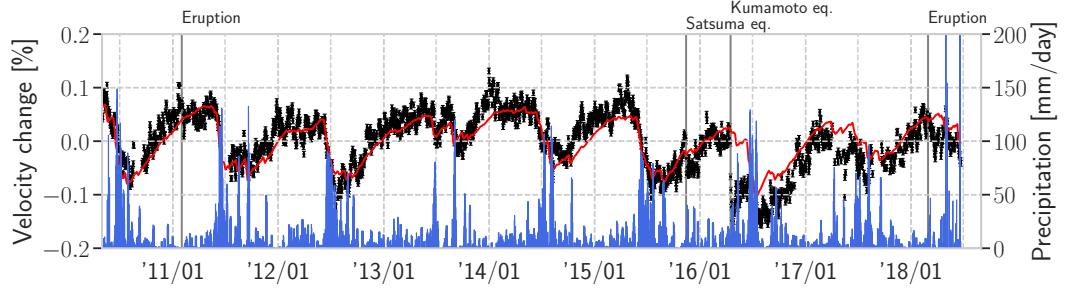


**Figure 4.** Row temporal changes of the pair between TKW and TKS with the prediction from the precipitation. The red line shows prediction by the precipitation model ( $\tau_g = 195$  days, and  $A_g = -6.84 \times 10^{-2}$  [%/m]), as described in the next section.

## 310 5 Maximum Likelihood Method for determining the hyper-parameters

311 In the previous section, we applied the extended Kalman filter, assuming that the  
 312 hyper-parameters were given. This section shows how to infer the hyper-parameters us-  
 313 ing the Maximum Likelihood Method, which is the second step of this technique.

314 The logarithmic likelihood  $\log L$  is given (e.g., Segall & Matthews, 1997; Durbin  
 315 & Koopman, 2012) by

$$316 \log L = -\frac{nN}{2} \log 2\pi - \frac{1}{2} \sum_{t=1}^n \left( \log(\det(\mathbf{F}_t)) + \hat{\mathbf{d}}_{t|t-1} \right), \quad (32)$$

317 where  $\mathbf{F}_t$  and  $\hat{\mathbf{d}}_{t|t-1}$  are given by,

$$318 \mathbf{F}_t \equiv h_0 \mathbf{I} + \mathbf{Z}_t \hat{\mathbf{P}}_{t|t-1} \mathbf{Z}_t^T, \quad (33)$$

319 and

$$320 \hat{\mathbf{d}}_{t|t-1} = \frac{1}{h_0^2} \left( h_0 \mathbf{v}_t^T \mathbf{v}_t - \mathbf{\Gamma}_t^T \left( \hat{\mathbf{P}}_{t|t-1}^{-1} + \frac{\mathbf{S}_t}{h_0} \right)^{-1} \right) \mathbf{\Gamma}_t, \quad (34)$$

321 respectively. We maximized the logarithmic likelihood  $\ln L$  with respect to the hyper-  
 322 parameters.

323 First, we describe how to model the hyper-parameters for explaining the precip-  
 324 itation effects and the reduction associated with the 2016 Kumamoto earthquake in the  
 325 following two subsections.

### 326 5.1 A model for the precipitation effects

327 Many researchers have reported periodic changes in seismic wave velocity associ-  
 328 ated with external sources such as tides (e.g., Yamamura et al., 2003; Takano et al., 2014,  
 329 2019), thermoelastic effects (e.g., Hillers et al., 2015; Wang et al., 2017) and snow load-  
 330 ing (e.g., Wang et al., 2017). The correspondence between strong rainfall and the seis-  
 331 mic velocity changes shown in Figure 4 suggest the dominance of the precipitation ef-  
 332 fect in this case. For modeling temporal changes of seismic wave velocity caused by pre-  
 333 cipitation, we considered two models: the model based on diffusion of a pore pressure  
 334 (Talwani et al., 2007; Rivet et al., 2015; Lecocq et al., 2017; Wang et al., 2017), and the  
 335 hydrological model (Sens-Schönfelder & Wegler, 2006).

336 The first model considered diffusion of pore pressure in a poroelastic medium with  
 337 a spatial scale of several km, which induces seismic velocity changes. This model also  
 338 required the sensitivity of seismic velocity to changes in pore pressure. As discussed in  
 339 section 7.2, the sensitivity is an order of magnitude smaller than the typical values. The  
 340 diffusion of pore pressure caused significant time delay, which is not consistent with the  
 341 observations in this study.

342 The second model related the seismic velocity to the groundwater level at a shal-  
 343 low depth due to the precipitation (Sens-Schönfelder & Wegler, 2006). Since the ground-  
 344 water level reaches a shallow depth of about 100 m in this region (Kagiyama et al., 1996;  
 345 Tsukamoto et al., 2018), we selected this model. The response of the groundwater level  
 346 to the precipitation is given by an exponential function (Sens-Schönfelder & Wegler, 2006;  
 347 Kim & Lekic, 2019). The amount of ground water storage  $g_t$  is given by

$$348 \quad g_t = \int_t^\infty (p(\tau) - \langle p \rangle) e^{-\frac{t-(\tau+\delta)}{\tau_g}} d\tau, \quad (35)$$

349 where  $p$  is daily precipitation,  $\delta$  shows delay time,  $\tau_g$  is the parameter describing the de-  
 350 cay,  $\langle p \rangle$  is the average precipitation throughout the analyzed time period. We modeled  
 351 that the explanatory variable for precipitation  $r_t$  is proportional to  $g_t$  as,

$$352 \quad r_t = A_g g_t = A_g \int_t^\infty (p(\tau) - \langle p \rangle) e^{-\frac{t-(\tau+\delta)}{\tau_g}} d\tau, \quad (36)$$

353 where  $A_g$  is the sensitivity of seismic wave velocity to the ground water level. Since there  
 354 exists ambiguity of the modeling,  $A_g$ ,  $\tau_g$ , and  $\delta$  should be constrained by the observa-  
 355 tions practically. We regard  $A_g$ ,  $\tau_g$  and  $\delta$  as hyper-parameters, and infer their values by  
 356 the Maximum Likelihood Method as shown later in this section.

357 To validate the second model quantitatively, we estimate the sensitivity  $A_g$  based  
 358 on a physical model: density perturbation due to groundwater levels causes the tempo-  
 359 ral change associated with precipitation. Since surface waves are dominant in the wave-  
 360 field in this frequency range, the depth sensitivity can be represented by that of the sur-  
 361 face wave for a 1-D medium (Obermann et al., 2013). We consider only Rayleigh waves  
 362 for simplicity, since a similar discussion can be applicable for Love waves. The phase ve-  
 363 locity perturbation of Rayleigh waves  $\delta c$  can be related to perturbations of density  $\rho$ ,  
 364 rigidity  $\mu$  and bulk modulus  $\kappa$  using the partial derivatives of phase velocity (Takeuchi  
 365 & Saito, 1972) as,

$$366 \quad \frac{\delta c}{c} = \int \left( K_\rho(z) \frac{\delta \rho(z)}{\rho(z)} + K_\kappa(z) \frac{\delta \kappa(z)}{\kappa(z)} + K_\mu(z) \frac{\delta \mu(z)}{\mu(z)} \right) dz, \quad (37)$$

367 where  $c$  is the phase velocity, and  $K_\rho$ ,  $K_\kappa$  and  $K_\mu$  are the Fréchet derivatives relating  
 368 the fractional perturbation of phase velocity  $\delta c/c$  to the fractional perturbations  $\delta \rho/\rho$ ,  
 369  $\delta \kappa/\kappa$ ,  $\delta \mu/\mu$ . The Fréchet derivatives are also known as the depth sensitivity kernels. Fig-  
 370 ure 5 shows an example of a depth sensitivity kernel at 0.6 Hz for the density and S-wave  
 371 velocity model shown in the figure.

372 Working under the assumption of (i) no temporal changes in the rigidity  $\mu$  and bulk  
 373 modulus  $\kappa$ , and (ii) the groundwater level of about 100 m, the temporal change  $r_t$  can  
 374 be estimated as,

$$375 \quad r_t = \int K_\rho(z) \frac{\delta \rho(z)}{\rho(z)} dz \approx K_\rho(0) \frac{\rho_w g t}{\rho(0)}, \quad (38)$$

376 where  $\rho_w$  is water density. Accordingly,  $A_g$  can be written by  $K_\rho(0) \frac{\rho_w}{\rho(0)}$ . For example,  
 377 with the model shown by Figure 5,  $A_g$  is estimated to be  $-7.5 \times 10^{-2}$  [%/m]. The con-  
 378 sistency between this estimate of  $-7.5 \times 10^{-2}$  [%/m] and the fitting result of  $-6.84 \times$   
 379  $10^{-2}$  [%/m] supports our model.

380 For estimation of the hyper-parameters, initial values are required. We estimated  
 381 them in two steps. First, the preliminary reference CCF,  $\hat{\gamma}_{t|n}$  was calculated for each sta-  
 382 tion pair. In equation (6),  $\mathbf{R}_t$  is assumed to be  $\mathbf{0}$ . Then,  $A_g$  and  $\tau_g$  were estimated by  
 383 calculating the least squared difference between  $r_t$  and  $\hat{\gamma}_{t|n}$ .  $\delta$  is fixed to 0. The red line

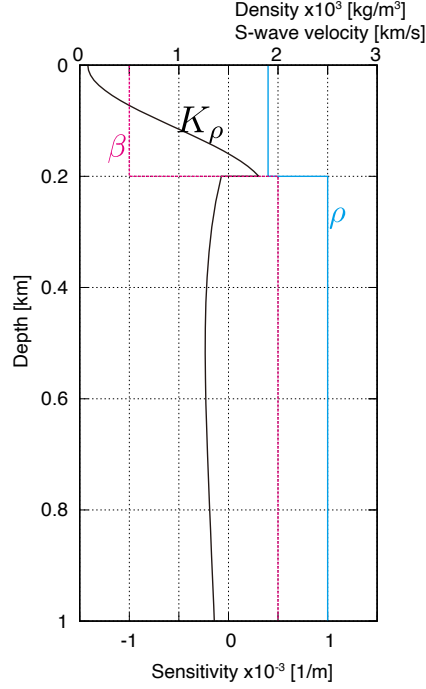


**Figure 5.** Depth sensitivity kernel to density perturbations at 0.6 Hz. The density  $\rho$  and the S-wave velocity  $\beta$  are plotted. P-wave velocities are 1.91 km/s from 0 to 0.2 km, and 4 km/s below 0.2 km.

384 in Figure 4 shows the initial estimate of a pair between TKW and TKS:  $\tau_g = 195$  days  
 385 and  $A_g = -6.84 \times 10^2$  [%/m]. This figure shows that the empirical model can predict  
 386 the seasonal variations well. To avoid the effects of the sudden drop due to the 2016 Ku-  
 387 mamoto earthquake, we used the data from before the earthquake in the estimation.

## 388 5.2 A model for the drops associated 2016 Kumamoto earthquake

389 After the reduction of the effect of precipitation with the tentative hyper-parameters,  
 390 the resultant temporal change shows sudden drops of seismic wave velocity associated  
 391 with the 2016 Kumamoto earthquake (Figure 6). Since the drop related to the Kumamoto  
 392 earthquake reaches 0.1 %, we modeled it by an exponential decay (Hobiger et al., 2016;  
 393 Gassenmeier et al., 2016; Sens-Schönfelder & Eulenfeld, 2019) as,

$$394 \quad e_t = A_t e^{\frac{t-t_0}{\tau_e}}, \quad (39)$$

395 where  $A_t$  is amplitude of the drop,  $t_0$  is the origin time of the Kumamoto earthquake,  
 396 and  $\tau_e$  is the decay time. We omitted a term of non-recovering coseismic velocity drops  
 397 (Hobiger et al., 2016) as the term could not be detected, as shown later (see Figure 10).

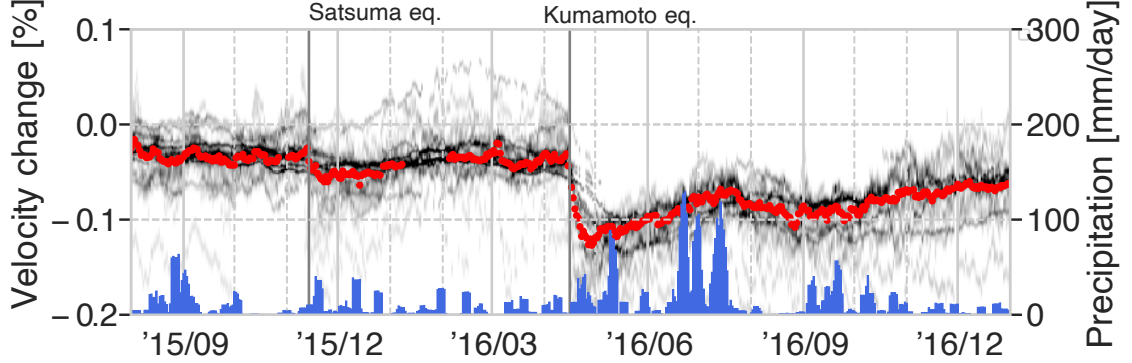


**Figure 6.** Velocity change associated with the 2016 Kumamoto earthquake. The seismic velocity drop when the earthquake occurred, and recovered over a time scale of three months. The grayscale shows marginal probability with all CCFs (see next section for details). The red dots show a median of all the measurements. The red dots also show a minor drop during the 2015 Satsuma earthquake.

### 398 5.3 Estimation of the hyper-parameters by Maximum Likelihood Method

399 To reduce the number of hyper-parameters, we assumed that the expected value  
 400 of the initial state value  $\mathbf{a}_1$  is given by  $(1, \gamma_1)$ , and the covariance matrix  $\mathbf{P}_1$  is equal to  
 401  $\mathbf{Q}_t$ .

402  $\ln L$  is a function of hyper-parameters  $\beta$ , where

$$403 \beta = (p_0, p_1, \tau_g, A_g, \delta, \gamma_1, A_e, \tau_e). \quad (40)$$

404 The logarithmic likelihood  $\ln L$  was maximized with respect to the hyper-parameters us-  
 405 ing a quasi-Newton method L-BFGS-B, which is a limited memory algorithm for solv-  
 406 ing large nonlinear optimization problems subject to simple bounds on the variables (Zhu  
 407 et al., 1994; Durbin & Koopman, 2012).

408 Figure 7 shows estimated hyper-parameters, which are well constrained by the ob-  
 409 servations. Figure 7 (b) shows a trend of decreasing sensitivity  $|A_g|$  with increasing de-  
 410 cay time  $\tau_g$ . This result suggest that the groundwater level changes at shallower depths

411 have shorter time decay time  $\tau_g$ , because the depth sensitivity kernel negatively increases  
 412 to the ground surface (Figure 5). Figure 7 (c), which compares  $A_e$  and  $\tau_e$ , shows the drop  
 413 when the earthquake becomes larger, decreasing the recovery time. This result suggests  
 414 that the stronger drop and shorter recovery occurred at shallower depths.

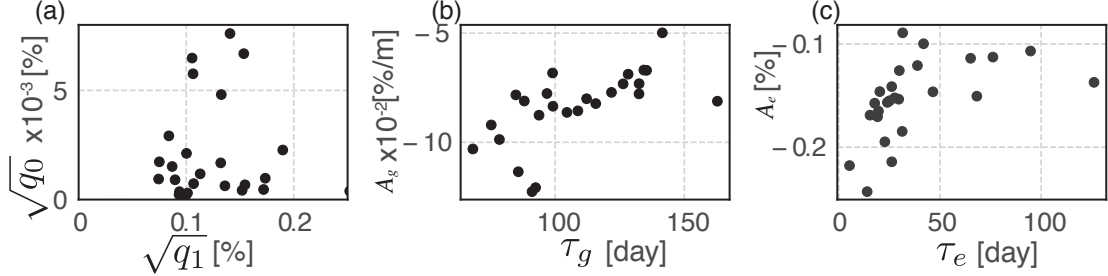


**Figure 7.** Estimated hyper-parameters. (a) scatter plot against standard deviations of the model:  $\sqrt{q_0}$  and  $\sqrt{q_1}$ , (b) scatter plot against hyper-parameters of precipitation effects:  $\tau_g$  and  $A_g$ , (c) scatter plot against hyper-parameters of the drop during the Kumamoto earthquake:  $A_e$  and  $\tau_e$ .

415 To determine how well the observations constrain the hyper-parameters  $\beta$ , we es-  
 416 timated the sensitivity of the logarithmic likelihood of the perturbations around the op-  
 417 timal value  $\beta^{opt}$ . Figure 8 shows an increment of logarithmic likelihood to the optimal  
 418 value of  $\Delta \ln L$  as a function of a hyper-parameter. We perturbed each hyper-parameter  
 419 within 50%, fixing all other hyper-parameters to the optimal values. Within this hyper-  
 420 parameter range, the minima of  $\Delta \ln L$  for all the hyper-parameters were smaller than  
 421 -1.

422 Here we considered the appropriate number of hyper-parameters using the Akaike  
 423 Information Criterion ( $AIC$ , Akaike, 1974) defined by

$$424 \quad AIC_K = -2 \ln \hat{L}_K + 2K, \quad (41)$$

425 where  $K$  is the number of hyper-parameters, and  $\ln \hat{L}_K$  represents the maximum like-  
 426 lihood for the  $K$  hyper-parameters. We choose the hyper-parameter if  $AIC_K$  decreases  
 427 with the addition of a new hyper-parameter: i.e. the increment  $\Delta AIC \equiv AIC_K - AIC_{K-1}$   
 428 is smaller than 0. Assuming that  $\ln \hat{L}_{K-1} - \ln \hat{L}_K$  can be approximated by  $\Delta \ln L$  shown  
 429 in Figure 8, the  $\Delta AIC$  is written by  $2(\Delta \ln L + 1)$ . The addition of a hyper-parameter  
 430 is appropriate if  $\Delta \ln L < -1$ . Assuming that the ambiguity of each parameter is about

431 50%, for example,  $\beta_i$  is fixed  $0.5\beta_i^{opt}$  as the a prior value. Since all the  $\Delta \ln L$  at  $\beta_i/\beta_i^{opt} =$   
 432 0.5 in Figure 8 are smaller than  $-1$ , all the hyper-parameters used to meet this condi-  
 433 tion. This choice of hyper-parameters also makes the iterations of the L-BFGS-B method  
 434 stable.

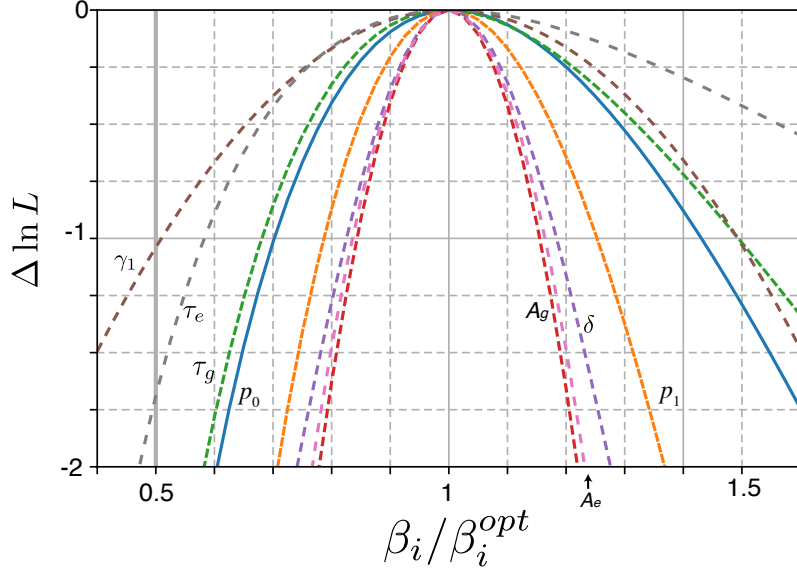


**Figure 8.** Logarithmic likelihood as a function of the normalized hyper-parameters. The horizontal axis shows relative value of hyper-parameters, and the vertical axis shows increments of logarithmic likelihood to the optimal value  $\ln L(\beta^{opt})$ . The corresponding hyper-parameters ( $\beta_i$ ) are also shown in this figure.

## 435 6 Temporal changes of seismic wave velocity

436 Using the inferred hyper-parameters, we estimated state variables for all pairs of  
 437 stations. Red lines in the upper triangular portion of Figure 9 show the total temporal  
 438 changes of seismic wave velocity  $\hat{\gamma}_{t|n} + r_t + e_t$ . The blue lines show only the explana-  
 439 tory parameters  $r_t + e_t$  for precipitation and the earthquake. The explanatory param-  
 440 eters can explain majority of the aspects of the estimated temporal changes.

441 The lower triangular portion of Figure 9 shows the resultant  $\hat{\alpha}_{t|n}$ . The blue lines  
 442 show the amplitude perturbations  $\hat{A}_{t|n}$ , which show the local minimum in 2015. High  
 443 activities of low-frequency volcanic tremor at Mt. Aso could distort the coherency (Kaneshima  
 444 et al., 1996; Hendriyana & Tsuji, 2019; Sandanbata et al., 2015). The red lines show seis-

445 mic velocity changes,  $\hat{\gamma}_{t|n}$ , after the subtraction of the explanatory variables. They show  
 446 a consistent long term variation with a time scale of about five years with an amplitude  
 447 of about 0.05 %. Although most station pairs do not show significant temporal changes  
 448 associated with the 2011 eruption, the pair between SMW and SMN shows a significant  
 449 drop in 2011. The upper triangular portion shows the precipitation effect and the drop  
 450 associated with the earthquake are well subtracted using the explanatory parameters.

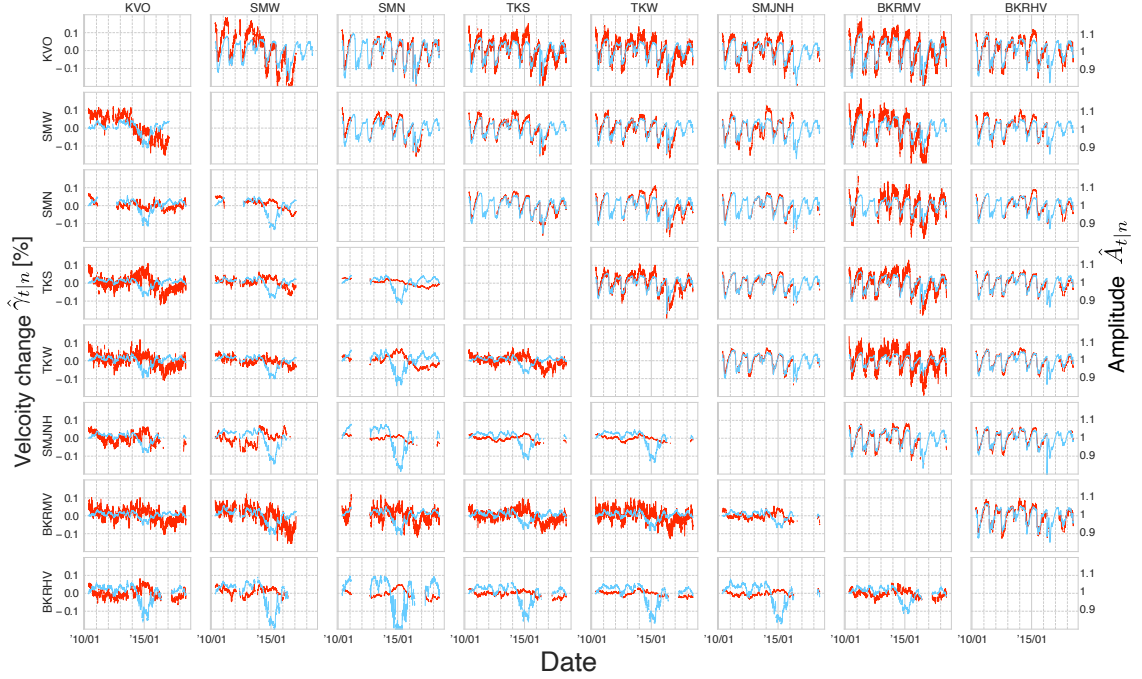


**Figure 9.** The lower triangular portion: resultant  $\hat{\alpha}_{t|n}$ . The red lines show seismic velocity change  $\hat{\gamma}_{t|n}$  within 0.1%. The blue lines show the amplitude perturbations  $\hat{A}_{t|n}$ , which show a local minimum in 2015. The upper triangular portion: Blue lines show estimated seismic velocity changes  $r_t + e_t$ , which explain the precipitation effect and the drop during the Kumamoto earthquake, whereas red ones show estimated whole seismic velocity changes  $\hat{\gamma}_{t|n} + r_t + e_t$ .

451 To discuss the long-term variations, we considered the marginal probability den-  
 452 sity with all the pairs of stations. Figure 10(a) shows the marginal probability density  
 453 over 8 years with an assumption that each measurement is independent. The probabil-  
 454 ity density  $f_t(\gamma)$  as a function of seismic velocity change  $\gamma$  is defined by

$$f_t(\gamma) \equiv \frac{1}{28} \sum_{j=1}^{28} \mathcal{N}(j\hat{\gamma}_{t|n}, j\hat{q}_{t|n}), \quad (42)$$

456 where  $\mathcal{N}$  represents normal distribution,  $\hat{\gamma}_{t|n}$  is the conditional mean of seismic veloc-  
 457 ity changes,  $\hat{q}_{t|n}$  is the corresponding conditional covariance,  $j$  indicates a station pair,  
 458 and 28 is the total number of station pairs. The marginal probability density (Figure  
 459 10(a)) shows no significant changes associated with the 2011 and 2018 eruptions of Shinmoe-  
 460 dake. However, areal strain calculated from GNSS observation shows inflation and de-  
 461 flation due to changes in the magma reservoir during the 2011 eruption, and the 2018  
 462 eruption (Nakao et al., 2013; Kozono et al., 2013; Yamada et al., 2019) (Figure 10(b)).  
 463 The areal strain also shows the static change due to the 2016 Kumamoto earthquake,  
 464 whereas  $f_t(\gamma)$  does not show significant static change.

465 Apart from jumps of the areal strain associated with the eruptions and the earth-  
 466 quake, both the seismic velocity changes and the areal strain (Figure 10) show tempo-  
 467 ral variations with a time scale of about one year with local maxima in January 2012 and  
 468 January 2013. After 2014, such temporal variations are no longer observed for both. One  
 469 possible origin of the variations is the long term variations in groundwater levels (e.g.,  
 470 Lecocq et al., 2017). When modeling groundwater level in equation (35), we assumed  
 471 constant drainage. Nevertheless, under realistic conditions, the drainage may change with  
 472 time. Since the areal strain also shows a similar undulation pattern from 2010 to 2013,  
 473 such a long-term variation may cause large scale deformations. The induced pore pres-  
 474 sure change (Talwani et al., 2007) at deeper depth, on the order of km, could also cause  
 475 seismic velocity changes (Wang et al., 2017; Rivet et al., 2015). In this study, however,  
 476 the hydrological data were insufficient to verify this hypothesis.

## 477 7 Discussions

478 In the following subsections, we discuss two specific events: the drop of seismic wave  
 479 velocity associated with the Kumamoto earthquake and the 2011 Shinmoe-dake erup-  
 480 tion. Based on the observed features, we discuss the magma pathway beneath Shinmoe-  
 481 dake.

### 482 7.1 The drop of seismic wave velocity when the Kumamoto earthquake

483 Our results show a sudden drop during the Kumamoto earthquake followed by a  
 484 recovery from 10 to 100 days (Figure 7). Since the probability density  $f_t(\gamma)$  does not show  
 485 non-recovering coseismic velocity drops due to the static areal-strain change (Figure 10),

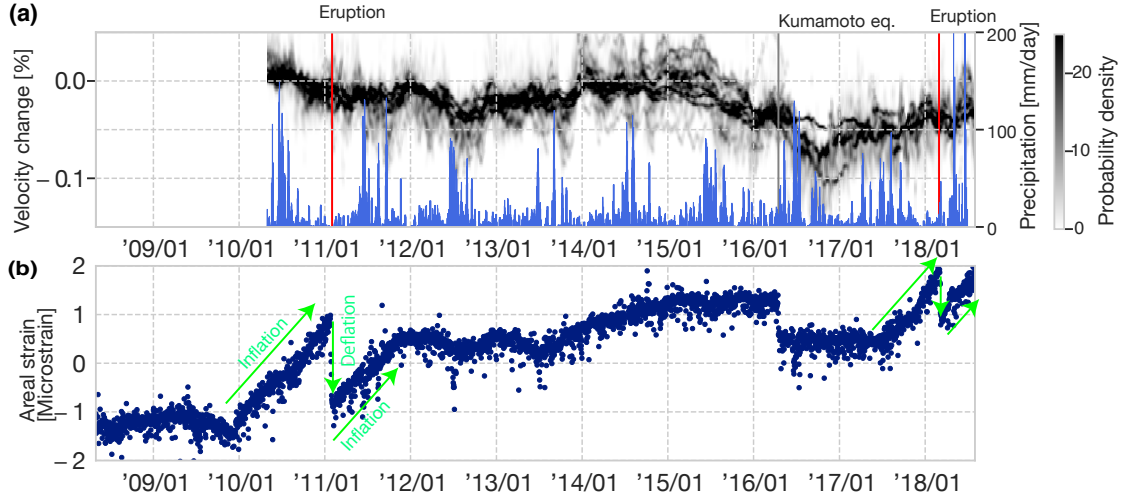


**Figure 10.** (a) Marginal probability density of all pairs of stations. The blue bars show daily precipitation data at the JMA meteorological station. The estimated seismic velocities scatter from Oct. 2014 to May 2015 when the activity of low frequency tremor at Mt. Aso occurs. (b) Areal strain calculated from three GEONET stations: Ebino, Miyakonojou2 and Makizono shown in Figure 1.

486 the observed static strain change could not be the dominant source. Near-surface dam-  
 487 age beyond the linear elastic regime could be a possible origin. For the discussion, we  
 488 compare the susceptibility, which is defined by the ratio between observed reductions in  
 489 seismic velocity and the estimated dynamic stress with that of the 2011 Tohoku earth-  
 490 quake (Brengruer et al., 2014).

491 We estimated the dynamic stress from the observed peak ground velocity (PGV)  
 492 (Gomberg & Agnew, 1996). PGV in this region was about 5 cm/s during the Kumamoto  
 493 earthquake, which was averaged over 3 components of PGV measured by the K-net, strong-  
 494 motion seismograph network. The dynamic stress  $\Delta\sigma \approx \mu v/c$  was estimated to be 0.5 MPa,  
 495 where  $\mu$  is the mean crustal shear modulus ( $\sim 30$  GPa),  $v$  is PGV, and  $c$  is the mean  
 496 wave phase velocity of the Rayleigh wave ( $\sim 3$  km/s) (Brengruer et al., 2014). The sus-  
 497 ceptibility (Brengruer et al., 2014), which is defined by the ratio between observed re-  
 498 ductions in seismic velocity  $\Delta c/c$  ( $\sim 2 \times 10^{-3}$ ) and the estimated dynamic stress 0.5 MPa,  
 499 was about  $4 \times 10^{-3} \text{ MPa}^{-1}$ . This value is larger than susceptibility in the Mt. Fuji area  
 500 and along the Tohoku volcanic during the Tohoku earthquake, whose value is about  $1.5 \times$

501  $10^{-3} \text{ MPa}^{-1}$  (Breguier et al., 2014). This observation suggests that the pressurized ge-  
 502 ofluid in the upper crust and/or near-surface is a possible origin for the seismic veloc-  
 503 ity changes.

504 We discuss the mechanism of the observed seismic velocity change as caused by the  
 505 pressurized fluid. The exponential decay time scales ranged from 10 to 100 days, sug-  
 506 gesting the lack of a relaxation process longer than 100 days (Snieder et al., 2017). The  
 507 estimation of relatively short time scales dismisses the mechanisms of post-seismic re-  
 508 laxation of stress (e.g., Breguier, Shapiro, et al., 2008) and diffusion of geofluid in the  
 509 crust (Wang et al., 2019). The absence of non-recovering coseismic velocity drop dur-  
 510 ing the 2016 Kumamoto earthquake suggests that the pressurization of geofluid in the  
 511 linear elastic regime is unlikely to be the origin. This hypothesis is also consistent with  
 512 the observation that the 2011 Tohoku earthquake did not trigger any volcanic and seis-  
 513 mic activities in this region (Miyazawa, 2011). Near-surface damage due to the strong  
 514 ground motions beyond the linear elastic regime, where rich groundwater exists, could  
 515 be a plausible origin.

## 516 **7.2 Temporal changes when the volcanic eruptions in 2011**

517 The probability density of all the station pairs  $f_t$  (Figure 10(a)) does not show any  
 518 temporal change associated with the volcanic eruptions from January 2011 to February  
 519 2011. However, geodetic observation showed the gradual magma intrusion over the time  
 520 scale of a year and the discharge during the eruption (see the areal strain in Figure 10(b)).  
 521 The geodetic source was located 5 km to the northwest of the summit at a depth of about  
 522 8 km (Nakao et al., 2013). Although the volumetric change caused enough strain (about  
 523 1.5 microstrains estimated from GNSS as shown by Figure 10) to cause the seismic ve-  
 524 locity change with a typical sensitivity of seismic velocity change in a linear elastic regime  
 525 (e.g., Takano et al., 2017), as discussed later, our results do not show a significant change.  
 526 These observations could provide a clue for inferring the state of the material in the up-  
 527 per crust.

528 Despite of the absence of observed temporal changes for most station pairs dur-  
 529 ing the 2011 eruption (Figure 9), one station pair close to the crater (SMW and SMN)  
 530 showed a significant drop of seismic velocity (red lines in Figure 11). Figure 11 shows  
 531 the resultant temporal variations between the station pair (SMW and SMN) from May

532 2010 to May 2011. The gradual drop of seismic velocity preceded the eruption by one  
 533 month. Since the station SMN was broken 10 days after the main phase of the 2011 erp-  
 534 tion, the post-eruption recovery cannot be discussed.

535 We discuss the 2011 Shimoedake-eruption based on the two observed temporal vari-  
 536 ations in seismic wave velocity: (i) no observed temporal variations with the one-year  
 537 inflation of the magma reservoir, (ii) only the station pair close to the crater detected  
 538 the gradual decrease preceding the eruption by one month.

539 First, we consider why the observation only shows temporal variation at one pair.  
 540 Figure 12 shows areal strain, induced by the point volumetric source, by deflation caused  
 541 by the migration of magma to the surface. The volumetric source modeled by Nakao et  
 542 al. (2013) was located at a point (longitude 130.831°E, latitude 31.942°N, depth 8.35 km),  
 543 which is about 6.9 km northwestern to Shinmoe-dake. The modeled volume change of  
 544 the deflation is  $13.35 \times 10^6 \text{ m}^3$ . This model can explain the GNSS observations during  
 545 the deflation in 2011: i.e., this model can explain the observed drop of areal strain based  
 546 on GNSS shown by Figure 10(b).

547 The typical areal strain at a depth of 3 km above the volumetric source is  $5 \times 10^{-6}$ ,  
 548 and the typical value of the bulk modulus at a depth of 3 km is 30 GPa. Since the cor-  
 549 responding stress change is  $1.5 \times 10^5 \text{ Pa}$ , the stress sensitivity of seismic velocity change  
 550 is estimated to be less than  $6 \times 10^{-10} \text{ Pa}^{-1}$ . As this estimated stress sensitivity is an  
 551 order of magnitude smaller than the past studies at the depth (Takano et al., 2017), our  
 552 results suggest that the crustal material has lower sensitivity to static stress changes in  
 553 a linear elastic regime than other regions. This observation is also consistent with that  
 554 the 2016 Kumamoto earthquake caused only recovering coseismic velocity drops due to  
 555 dynamic stress but no permanent ones in response to static changes in areal strain (Fig-  
 556 ure 10). The observed lack of sensitivity is also consistent with our model of precipita-  
 557 tion effects, which does not require stress sensitivity of the seismic velocity.

558 One possible interpretation of the observed low sensitivity or lack of sensitivity could  
 559 be related to the aspect ratio of crack and/or fluid inclusion of the medium. The low sen-  
 560 sitivity suggests that the shape of cracks could be circular (Shapiro, 2003). The P-wave  
 561 velocity at 3 km is about 5.5 km/s (Tomatsu et al., 2001), and the S-wave velocity is ap-  
 562 proximately 3.1 km/s (Nagaoka, 2020), suggesting that fraction of the geofluid and crack  
 563 density should be small. The inclusions of the geofluid could also be isolated because the

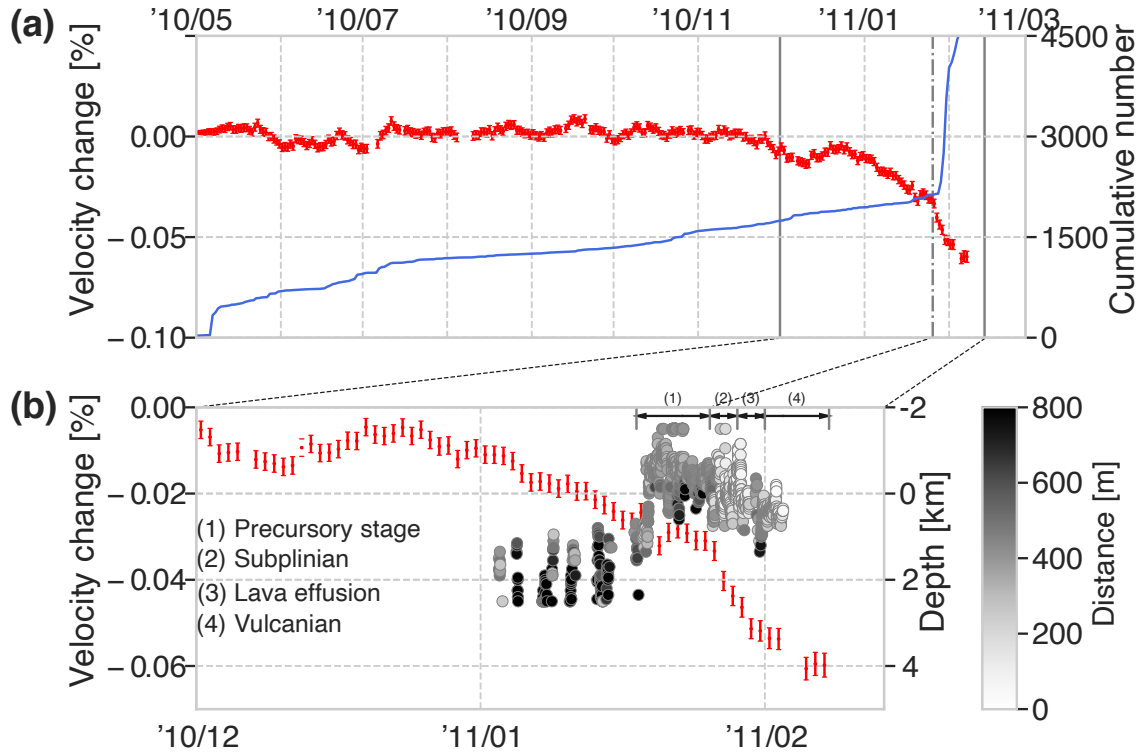


**Figure 11.** (a) Seismic velocity changes  $\hat{\gamma}_{t_n}$  for the pair between SMN and SMW shown by red bars. The station SMN was damaged during the eruption. The line in sky blue shows the cumulative number of volcanic earthquakes determined by JMA below Shinmoe-dake. (b) Enlarged figure from October 1st, 2010 to February 14th, 2011. The panel also shows the depth of volcanic tremor (Ichihara & Matsumoto, 2017). The color of a circle shows the horizontal distance from the center of the summit to the hypocenter. Four periods: (1) Precursory stage, (2) Sub-Plinian, (3) Lava effusion, and (4) Vulcanian (e.g., Nakada et al., 2013; Kozono et al., 2013) are also shown.

564 3-D inversion of the anomalous magnetotelluric data in this region showed a highly re-  
 565 sistive body above the volumetric source (Aizawa et al., 2014).

566 Next, we considered the spatial localization of the gradual decrease near the crater  
 567 precedes the eruption by one month. For simplicity, we considered the homogeneous medium  
 568 with seismic velocity  $c$  of 2 km/s, which correspond to a typical group velocity of Rayleigh  
 569 waves. We evaluated the sensitivity kernel of the travel time from a point  $\mathbf{s}_1$  to a point  
 570  $\mathbf{s}_2$  for local changes of seismic velocities as

$$571 \quad \left. \frac{\delta c(t)}{c} \right|_{app} = \frac{1}{ct} \int_S K(\mathbf{s}_1, \mathbf{s}_2, \mathbf{r}, t) \delta v(\mathbf{r}) dS(\mathbf{r}), \quad (43)$$

572 where  $\left. \frac{\delta c(t)}{c} \right|_{app}$  is apparent velocity change, which corresponds to the measurement,  $t$   
 573 is travel time,  $\delta v(\mathbf{r})$  is perturbation of the seismic velocity at a point  $\mathbf{r}$ ,  $S$  represents the  
 574 whole surface area, and  $K$  is a sensitivity kernel (Pacheco & Snieder, 2005) given by,

$$575 \quad K(\mathbf{s}_1, \mathbf{s}_2, \mathbf{r}, t) = \frac{\int_0^t p(\mathbf{s}_1, \mathbf{r}, t') p(\mathbf{r}, \mathbf{s}_2, t - t') dt'}{p(\mathbf{s}_1, \mathbf{s}_2, t)}, \quad (44)$$

576 where  $p(\mathbf{s}_1, \mathbf{s}_2, t)$  is the probability density that the wave traveled from  $\mathbf{s}_1$  to  $\mathbf{s}_2$  during  
 577 time  $t$  (Machacca et al., 2019): i.e.  $p(\mathbf{s}_1, \mathbf{r}, t)$  satisfies the normalization condition given  
 578 by,

$$579 \quad \int_S p(\mathbf{s}_1, \mathbf{r}, t) dS(\mathbf{r}) = 1. \quad (45)$$

580 Here  $p$  is given the analytic form of the radiative transfer for isotropic scattering in 2-  
 581 D (Obermann et al., 2013) as,

$$582 \quad p(r, t) = \frac{\exp\left(-\frac{ct}{l}\right)}{2\pi r} \delta(ct-r) + \frac{1}{2\pi lct} \left(1 - \frac{r^2}{c^2 t^2}\right)^{-1/2} \exp\left(\frac{\sqrt{c^2 t^2 - r^2} - ct}{l}\right) H(ct-r), \quad (46)$$

583 where  $l$  is the scattering mean free path of 5000 m,  $r$  is the distance between  $\mathbf{s}_1$  and  $\mathbf{s}_2$ ,  
 584 and  $H$  is the Heaviside step function. Figure 12 (a) shows the sensitivity kernel at the  
 585 lapse time  $t = 60$  s, which shows two local maxima at the stations. If the damaged area  
 586 is 1 km at the Shinmoe-dake, which is about twice as the crater size, the velocity drop  
 587 within the area is estimated to be about 5%. A trade-off exists between  $\delta c$  and the dam-  
 588 aged area.

589 We considered three possible origins of the localized seismic velocity changes: (i)  
 590 stress sensitivity of the edifice in a linear elastic regime, (ii) density perturbation due to  
 591 the magma intrusion, and (iii) damage accumulation near the crater. We already showed  
 592 the stress sensitivity in this region is small although past studies (e.g., Sens-Schönfelder  
 593 et al., 2014) have shown that stress changes due to the increased pressure of the magma

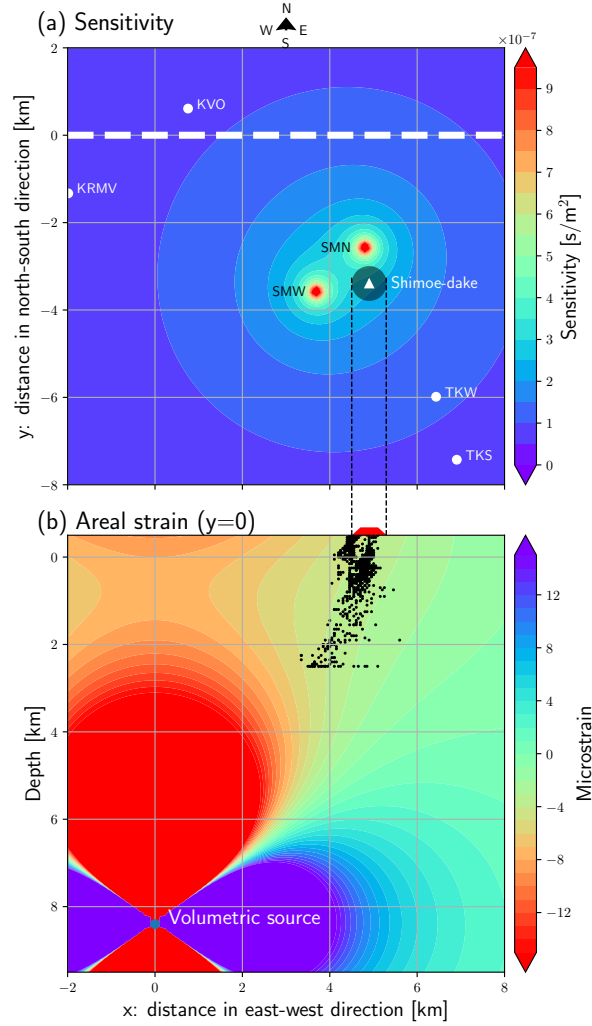


**Figure 12.** (a) Sensitivity kernel (Pacheco & Snieder, 2005; Obermann et al., 2013) at lapse time of 60 s. The scattering mean free path is assumed to be 5000 m. (b): Areal strain induced by the point volumetric source. The model (Nakao et al., 2013) is based on geodetic observation. This panel also shows hypocenters of volcanic tremors given by Ichihara and Matsumoto (2017). Although the hypocenters below 1 km were shifted in a westward direction, the shift might be caused by limited station coverage. We calculated the strain caused by the volumetric source using an inflation point source model (Okada, 1992) in a 3D elastic half-space with the rigidity of 10 GPa, and Poisson’s ratio of 0.25. For simplicity, we assumed that the height of the surface in this area is fixed to 0.5 km about sea level.

594 reservoir could cause the observable seismic velocity change. Moreover, no other infla-  
595 tion/deflation sources were observed before the 2011 Shinmoe-dake eruption. Next, we  
596 considered density perturbation, as in the case of the precipitation effect. Kozono et al.  
597 (2013) estimated the erupted volume based on geodetic and satellite observations. The  
598 total extruded volume of density rock equivalent was estimated to about  $3 \times 10^7 \text{ m}^3$ ,  
599 and the density was  $2500 \text{ kg/m}^3$ . In order to constrain the upper limit of seismic veloc-  
600 ity reduction due the density perturbation, we assumed that the magma stored at a depth  
601 shallower than 0.6 km where Rayleigh wave has the greater sensitivity (Figure 5). The  
602 equation (38) leads to the upper limit of about 0.6% drop in seismic velocity, which is  
603 significantly smaller than our observations (5%). Therefore we conclude that the observed  
604 seismic velocity drop with a time scale of about one month near the crater could be caused  
605 by cumulative damage beyond the linear elastic regime, induced by the pressure exerted  
606 by the magma reservoir on the edifice (Olivier et al., 2019).

607 The location of the volcanic tremor (TR) source also gives us a clue as to the magma  
608 or gas movement before the main eruption. Ichihara and Matsumoto (2017) located TR  
609 sources from seven stations recording continuous volcanic tremor before and during the  
610 sub-Plinian eruptions using the amplitude distribution. Figure 11(b) shows the source  
611 depth of TR from January 3rd, 2011, to February 2nd, 2011. Prior to January 2011, the  
612 TR amplitudes were too small to locate. Before the precursory stage of the eruption, the  
613 source depths were approximately 2 km. With increased damage, the source depth mi-  
614 grated upward to around sea level when the precursory stage was initiated. When the  
615 sub-Plinian eruption started, the decreasing rate of seismic velocity changes became steeper.  
616 This observation suggests that the magma migration from 2 km to the surface increased  
617 the damage of the sub-surface material. Figure 12(b) shows the depth section of the source  
618 locations. They also support the vertical magma migration beneath the summit. The  
619 sources below 1 km could be biased in the western direction, due to the limited station  
620 distribution.

621 Ambient noise tomography in this region (Nagaoka, 2020) revealed the magma reser-  
622 voir imaged as a low S-wave velocity body with a strong radial anisotropy of up to 30%.  
623 It was located just below the geodetic source, and the horizontal scale was about 15 km  
624 (Figure 13). Horizontally multilayered sills can explain the strong radial anisotropy with  
625 and without partial melts. The connection between the sills can enable the horizontal  
626 magma migration from the magma reservoir to Shinmoe-dake. The geochemical anal-

627 ysis (Nakada et al., 2013; Suzuki et al., 2013) showed the basaltic magma was stored at  
 628 the magma reservoir. The viscosity is low enough to develop the sill complex, and the  
 629 mobility is high during the eruption. In January 2011, due to damage, the pressuriza-  
 630 tion of the magma began to decrease the seismic velocity gradually. The pressurization  
 631 also activated TR activity at depth of 2 km (Figure 13(a)). During this stage, the sili-  
 632 cific magma was mixed with the basaltic magma (Suzuki et al., 2013). Since the viscos-  
 633 ity of the silicic magma is estimated to be high (about  $1.2 \times 10^6$  Pa·s, Suzuki et al., 2013),  
 634 the magma fluid could be isolated.

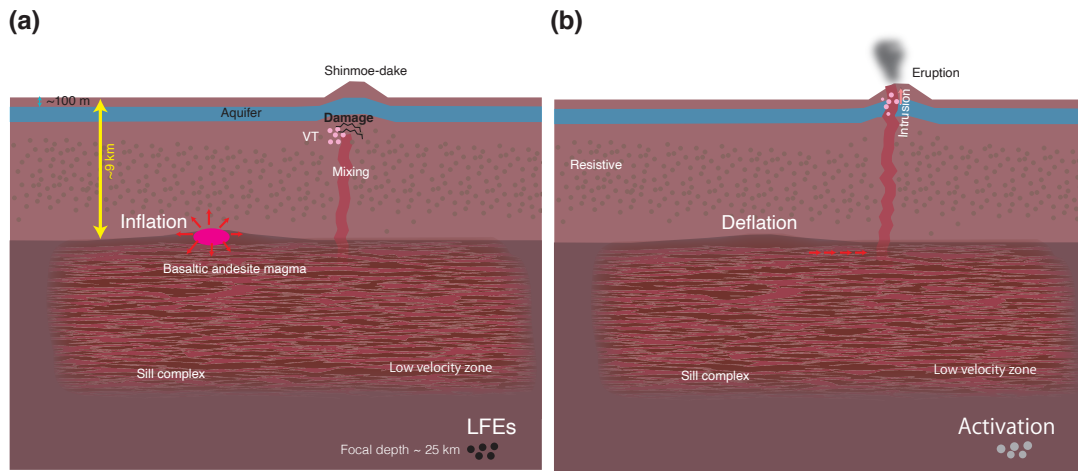


**Figure 13.** Schematic of the 2011 eruption: (a) from one month before until just before the eruption, and (b) during the eruption. LFEs represent low frequency earthquakes (Kurihara et al., 2019), and TR represents volcanic tremor (Ichihara & Matsumoto, 2017).

## 635 8 Conclusions

636 In this study, seismic interferometry was applied to a seismic array around Shinmoe-  
 637 dake to monitor the seismic velocity change for eight years from May 2010 to April 2018.  
 638 We applied the stretching method (Sens-Schönfelder & Wegler, 2006) for a cross-correlation  
 639 function calculated for each pair of stations using continuous ambient noise data. To sep-  
 640 arate the variations of volcanic origin from environmental variations, we developed a new  
 641 technique based on a state-space model: the parameters (e.g., seismic velocity change)  
 642 were estimated by an extended Kalman filter, and the hyper-parameters (the seismic re-  
 643 sponse to the precipitation, the response to the Kumamoto earthquake, and covariances

644 of the parameters) were estimated by the Maximum Likelihood Method. The resultant  
645 seismic velocity changes show clear seasonal variation originating from precipitation as  
646 well as a drop associated with the 2016 Kumamoto earthquake.

647 After the effects of precipitation and the earthquake were subtracted, most of the  
648 seismic velocity changes did not show any changes associated with the eruptions. Since  
649 the strain changes caused by the volumetric change during the 2011 eruption (Nakao et  
650 al., 2013) were about five microstrains at depths from 0 to 2 km above the source, the  
651 stress sensitivity of the seismic velocity in a linear elastic regime was significantly smaller  
652 than the other areas (e.g. Takano et al., 2017). The observed lack of sensitivity suggests  
653 the smaller aspect ratio of crack and less fluid inclusion of the upper crust (Shapiro, 2003),  
654 which is consistent with the highly resistive body above the volumetric source (Aizawa  
655 et al., 2014). The P-wave velocity at 3 km is about 5.5 km/s (Tomatsu et al., 2001), and  
656 the S-wave velocity is about 3.1 km/s (Nagaoka, 2020), indicating small melt fraction  
657 and crack density.

658 Only one station pair located in the neighborhood of the crater showed a gradual  
659 decrease in seismic velocity, which preceded the eruption by one month. The maximum  
660 drop of the seismic velocity was about 0.05% during the 2011 eruption. The sensitivity  
661 kernel (Pacheco & Snieder, 2005) of this observation suggests that the seismic wave drop  
662 of about 5% was localized at the crater with a spatial dimension of about one km<sup>2</sup>. In  
663 this region, P wave travel time tomography revealed a pipe-like structure of high-velocity  
664 under the summit craters from 1.5 to 0.5 km below sea level (Tomatsu et al., 2001). The  
665 fluid intrusion started to damage the high-velocity pipe structure one month before the  
666 eruption. Until January 16th 2011, the source depths of TR were around 2 km (Ichihara  
667 & Matsumoto, 2017) although the TR amplitudes were too small to locate before Jan-  
668 uary 2011. With increasing damage, the source depth migrated upward to around sea  
669 level when the precursory stage started on January 16th. Then, the magma migrated  
670 from the depth of 2 km to the surface. The magma migrated vertically from the reser-  
671 voir imaged as a low S-wave velocity body just below the geodetic source.

## 672 **Acknowledgments**

673 I am grateful to people for maintaining the networks and making the data readily avail-  
674 able. This work was supported by JSPS KAKENHI Grant Number JP17H02950 and JP17K05625.  
675 We used data from F-net ([doi.org/10.17598/nied.0005](https://doi.org/10.17598/nied.0005)), Hi-net ([doi.org/10.17598/](https://doi.org/10.17598/)

676 nied.0003), V-net ([doi.org/10.17598/nied.0006](https://doi.org/10.17598/nied.0006)) and K-net ([doi.org/10.17598/nied.0004](https://doi.org/10.17598/nied.0004)), which are managed by the National Research Institute for Earth Science  
 677 and Disaster Prevention (NIED), Japan. In situ precipitation observations were obtained  
 678 from the Automated Meteorological Data Acquisition System (AMeDAS) of the Japan  
 679 Meteorological Agency (JMA) are available at [http://www.data.jma.go.jp/obd/stats/](http://www.data.jma.go.jp/obd/stats/etrn/index.php)  
 680 [etrn/index.php](http://www.data.jma.go.jp/obd/stats/etrn/index.php) (in Japanese). F3 solutions of GNSS data are provided by Geospatial  
 681 Information Authority of Japan (<http://www.gsi.go.jp>). This research made use of  
 682 ObsPy (Krischer et al., 2015), NumPy (Van Der Walt et al., 2011) and SciPy (Virtanen  
 683 et al., 2019). Figure 1 was prepared with GMT programs (Wessel et al., 2013). We thank  
 684 M. Takeo, Y. Takei and T. Ohminato for the valuable discussions.  
 685

686 **Data and materials availability:** The data useful to reproduce all the figures  
 687 will be uploaded to an open repository after revision of the paper and before acceptance  
 688 for publication in accordance with the AGU guidelines.

## 689 References

- 690 Aizawa, K., Koyama, T., Hase, H., Uyeshima, M., Kanda, W., Utsugi, M., ...  
 691 Ogawa, Y. (2014). Three-dimensional resistivity structure and magma plumbing  
 692 system of the Kirishima Volcanoes as inferred from broadband magnetotelluric  
 693 data. *Journal of Geophysical Research: Solid Earth*, *119*(1), 198–215. doi:  
 694 10.1002/2013JB010682
- 695 Akaike, H. (1974). A New Look at the Statistical Model Identification. *IEEE*  
 696 *Transactions on Automatic Control*, *19*(6), 716–723. doi: 10.1109/TAC.1974  
 697 .1100705
- 698 Aoki, Y., Segall, P., Kato, T., Cervelli, P., & Shimada, S. (1999). Imaging magma  
 699 transport during the 1997 seismic swarm off the Izu Peninsula, Japan. *Science*,  
 700 *286*(5441), 927–930. doi: 10.1126/science.286.5441.927
- 701 Bensen, G. D., Ritzwoller, M. H., Barmin, M. P., Levshin, A. L., Lin, F., Moschetti,  
 702 M. P., ... Yang, Y. (2007). Processing seismic ambient noise data to obtain re-  
 703 liable broad-band surface wave dispersion measurements. *Geophysical Journal*  
 704 *International*, *169*(3), 1239–1260. doi: 10.1111/j.1365-246X.2007.03374.x
- 705 Brenguier, F., Campillo, M., Hadziioannou, C., Shapiro, N., Nadeau, R. M., &  
 706 Larose, E. (2008). Postseismic relaxation along the san andreas fault at  
 707 parkfield from continuous seismological observations. *Science*, *321*(5895),

- 708 1478–1481.
- 709 Brenguier, F., Campillo, M., Takeda, T., Aoki, Y., Shapiro, N. M., Briand, X.,  
710 ... Miyake, H. (2014). Mapping pressurized volcanic fluids from in-  
711 duced crustal seismic velocity drops. *Science*, *345*(6192), 80–82. doi:  
712 10.1126/science.1254073
- 713 Brenguier, F., Rivet, D., Obermann, A., Nakata, N., Bouo e, P., Lecocq, T., ...  
714 Shapiro, N. (2016). 4-D noise-based seismology at volcanoes: Ongoing ef-  
715 forts and perspectives. *Journal of Volcanology and Geothermal Research*, *321*,  
716 182–195. doi: 10.1016/j.jvolgeores.2016.04.036
- 717 Brenguier, F., Shapiro, N. M., Campillo, M., Ferrazzini, V., Duputel, Z., Coutant,  
718 O., & Necessian, A. (2008). Towards forecasting volcanic eruptions using  
719 seismic noise. *Nature Geoscience*, *1*(2), 126–130. doi: 10.1038/ngeo104
- 720 Budi-Santoso, A., & Lesage, P. (2016). Velocity variations associated with the large  
721 2010 eruption of Merapi volcano, Java, retrieved from seismic multiplets and  
722 ambient noise cross-correlation. *Geophysical Journal International*, *206*(1),  
723 221–240. doi: 10.1093/gji/ggw145
- 724 Colombi, A., Chaput, J., Brenguier, F., Hillers, G., Roux, P., & Campillo, M.  
725 (2014). On the temporal stability of the coda of ambient noise correla-  
726 tions. *Comptes Rendus - Geoscience*, *346*(11-12), 307–316. doi: 10.1016/  
727 j.crte.2014.10.002
- 728 Donaldson, C., Caudron, C., Green, R. G., Thelen, W. A., & White, R. S. (2017).  
729 Relative seismic velocity variations correlate with deformation at Kilauea vol-  
730 cano. *Science Advances*, *3*(6), e1700219. doi: 10.1126/sciadv.1700219
- 731 Durbin, J., & Koopman, S. J. (2012). *Time Series Analysis by State Space Methods*  
732 (Second ed.). Oxford University Press. doi: 10.1093/acprof:oso/9780199641178  
733 .001.0001
- 734 Farr, T. G., Rosen, P. A., Caro, E., Crippen, R., Duren, R., Hensley, S., ... Alsdorf,  
735 D. (2007). The Shuttle Radar Topography Mission. *Review of Geophysics*,  
736 *45*(2), RG2004. doi: 10.1029/2005RG000183
- 737 Gassenmeier, M., Sens-Sch onfelder, C., Eulenfeld, T., Bartsch, M., Victor, P.,  
738 Tilmann, F., & Korn, M. (2016). Field observations of seismic velocity  
739 changes caused by shaking-induced damage and healing due to mesoscopic  
740 nonlinearity. *Geophysical Journal International*, *204*(3), 1490–1502. doi:

- 741 10.1093/gji/ggv529
- 742 Gomberg, J., & Agnew, D. (1996). The accuracy of seismic estimates of dynamic  
743 strains: An evaluation using strainmeter and seismometer data from Piñon  
744 Flat Observatory, California. *Bulletin of the Seismological Society of America*,  
745 *86*(1 SUPPL. A), 212–220.
- 746 Hendriyana, A., & Tsuji, T. (2019). Migration of Very Long Period Seismicity at  
747 Aso Volcano, Japan, Associated With the 2016 Kumamoto Earthquake. *Geo-*  
748 *physical Research Letters*, *46*(15), 8763–8771. doi: 10.1029/2019GL082645
- 749 Hillers, G., Ben-Zion, Y., Campillo, M., & Zigone, D. (2015). Seasonal varia-  
750 tions of seismic velocities in the San Jacinto fault area observed with ambient  
751 seismic noise. *Geophysical Journal International*, *202*(2), 920–932. doi:  
752 10.1093/gji/ggv151
- 753 Hobiger, M., Wegler, U., Shiomi, K., & Nakahara, H. (2016). Coseismic and post-  
754 seismic velocity changes detected by passive image interferometry: Comparison  
755 of one great and five strong earthquakes in Japan. *Geophysical Journal Inter-*  
756 *national*, *205*(2), 1053–1073. doi: 10.1093/gji/ggw066
- 757 Ichihara, M., & Matsumoto, S. (2017). Relative Source Locations of Contin-  
758 uous Tremor Before and After the Subplinian Events at Shinmoe-dake,  
759 in 2011. *Geophysical Research Letters*, *44*(21), 10,871–10,877. doi:  
760 10.1002/2017GL075293
- 761 Kagiyama, T., Utada, H., Uyeshima, M., Masutani, F., Kanda, W., Tanaka, Y., ...  
762 Mishina, M. (1996). Resistivity Structure of the Central and the Southeastern  
763 Part of Kirishima Volcanoes. *Bulltin of the volcanological society of Japan*,  
764 *41*(5), 215–225. doi: 10.18940/kazan.41.5.215
- 765 Kaneshima, S., Kawakatsu, H., Matsubayashi, H., Sudo, Y., Tsutsui, T., Ohminato,  
766 T., ... Iidaka, T. (1996). Mechanism of Phreatic Eruptions at Aso Volcano  
767 Inferred from Near-Field Broadband Seismic Observations. *Science*, *273*(5275),  
768 643–645. doi: 10.1126/science.273.5275.643
- 769 Kato, A., Nakamura, K., & Hiyama, Y. (2016). The 2016 Kumamoto earthquake  
770 sequence. *Proceedings of the Japan Academy Series B: Physical and Biological*  
771 *Sciences*, *92*(8), 358–371. doi: 10.2183/pjab.92.359
- 772 Kim, D., & Lekic, V. (2019). Groundwater Variations From Autocorrelation and  
773 Receiver Functions. *Geophysical Research Letters*, 722–729. doi: 10.1029/

- 774 2019GL084719
- 775 Kozono, T., Ueda, H., Ozawa, T., Koyaguchi, T., Fujita, E., Tomiya, A., & Suzuki,  
776 Y. J. (2013). Magma discharge variations during the 2011 eruptions of  
777 Shinmoe-dake volcano, Japan, revealed by geodetic and satellite observations.  
778 *Bull. Volcanol.*, *75*(3), 1–13. doi: 10.1007/s00445-013-0695-4
- 779 Krischer, L., Megies, T., Barsch, R., Beyreuther, M., Lecocq, T., Caudron, C., &  
780 Wassermann, J. (2015). ObsPy: A bridge for seismology into the scien-  
781 tific Python ecosystem. *Computational Science and Discovery*, *8*(1). doi:  
782 10.1088/1749-4699/8/1/014003
- 783 Kurihara, R., Obara, K., Takeo, A., & Tanaka, Y. (2019). Deep Low-Frequency  
784 Earthquakes Associated With the Eruptions of Shinmoe-dake in KirishimaVol-  
785 canoes. *Journal of Geophysical Research: Solid Earth*, 2019JB018032. doi:  
786 10.1029/2019JB018032
- 787 Lecocq, T., Longuevergne, L., Pedersen, H. A., Brenguier, F., & Stammer, K.  
788 (2017). Monitoring ground water storage at mesoscale using seismic noise:  
789 30 years of continuous observation and thermo-elastic and hydrological model-  
790 ing. *Sci. Rep.*, *7*(1), 1–16. doi: 10.1038/s41598-017-14468-9
- 791 Machacca, R., Lesage, P., Larose, E., Lacroix, P., & Anccasi, R. (2019). De-  
792 tection of pre-eruptive seismic velocity variations at an andesitic volcano  
793 using ambient noise correlation on 3-component stations: Ubinas vol-  
794 cano, Peru, 2014. *Journal of Volcanology and Geothermal Research*. doi:  
795 10.1016/j.jvolgeores.2019.05.014
- 796 Maeda, T., Obara, K., Furumura, T., & Saito, T. (2011). Interference of long-period  
797 seismic wavefield observed by dense hi-net array in japan. *Journal of Geophysi-  
798 cal Research*, *116*.
- 799 Miyazawa, M. (2011). Propagation of an earthquake triggering front from the 2011  
800 Tohoku-Oki earthquake. *Geophysical Research Letters*, *38*(23), n/a–n/a. doi:  
801 10.1029/2011GL049795
- 802 Nagaoka, Y. (2020). *Study on seismic velocity structure beneath active volcanoes by  
803 seismic interferometry* (PhD). The university of Tokyo.
- 804 Nagaoka, Y., Nishida, K., Aoki, Y., & Takeo, M. (2010). Temporal change of phase  
805 velocity beneath Mt. Asama, Japan, inferred from coda wave interferometry.  
806 *Geophysical Research Letters*, *37*(22), 1–5. doi: 10.1029/2010GL045289

- 807 Nakada, S., Nagai, M., Kaneko, T., Suzuki, Y., & Maeno, F. (2013). The outline  
808 of the 2011 eruption at Shinmoe-dake (Kirishima), Japan. *Earth, Planets and*  
809 *Space*, *65*(6), 475–488. doi: 10.5047/eps.2013.03.016
- 810 Nakamichi, H., Yamanaka, Y., Terakawa, T., Horikawa, S., Okuda, T., & Ya-  
811 mazaki, F. (2013). Continuous long-term array analysis of seismic records  
812 observed during the 2011 Shinmoedake eruption activity of Kirishima vol-  
813 cano, southwest Japan. *Earth, Planets and Space*, *65*(6), 551–562. doi:  
814 10.5047/eps.2013.03.002
- 815 Nakao, S., Morita, Y., Yakiwara, H., Oikawa, J., Ueda, H., Takahashi, H., . . . Iguchi,  
816 M. (2013). Volume change of the magma reservoir relating to the 2011  
817 Kirishima Shinmoe-dake eruption—Charging, discharging and recharging  
818 process inferred from GPS measurements. *Earth, Planets and Space*, *65*(6),  
819 505–515. doi: 10.5047/eps.2013.05.017
- 820 Nimiya, H., Ikeda, T., & Tsuji, T. (2017). Spatial and temporal seismic velocity  
821 changes on Kyushu Island during the 2016 Kumamoto earthquake. *Science Ad-*  
822 *vances*, *3*(11), e1700813. doi: 10.1126/sciadv.1700813
- 823 Nishida, K., Kawakatsu, H., & Obara, K. (2008). Three-dimensional crustal S wave  
824 velocity structure in Japan using microseismic data recorded by Hi-net tilt-  
825 meters. *Journal of Geophysical Research: Solid Earth*, *113*(B10), B10302. doi:  
826 10.1029/2007JB005395
- 827 Niu, F., Silver, P. G., Daley, T. M., Cheng, X., & Majer, E. L. (2008). Preseismic  
828 velocity changes observed from active source monitoring at the parkfield safod  
829 drill site. *Nature*, *454*(7201), 204.
- 830 Obermann, A., & Hillers, G. (2019). Chapter Two - Seismic time-lapse interferom-  
831 etry across scales. In C. Schmelzbach (Ed.), *Advances in seismology* (Vol. 60,  
832 pp. 65–143). Elsevier. doi: 10.1016/bs.agph.2019.06.001
- 833 Obermann, A., Planes, T., Larose, E., Sens-Schonfelder, C., & Campillo, M. (2013).  
834 Depth sensitivity of seismic coda waves to velocity perturbations in an elastic  
835 heterogeneous medium. *Geophysical Journal International*, *194*(1), 372–382.  
836 doi: 10.1093/gji/ggt043
- 837 Ogiso, M., Yomogida, K., & Katsumata, K. (2005). Recursive travel-time inver-  
838 sion: A tool for real-time seismic tomography. *Earth, Planets Sp.*, *57*(6), 477–  
839 489. doi: 10.1186/BF03352582

- 840 Okada, Y. (1992). Internal deformation due to shear and tensile faults in a half-  
841 space. *Bulletin - Seismological Society of America*, *82*(2), 1018–1040.
- 842 Olivier, G., Brenguier, F., Carey, R., Okubo, P., & Donaldson, C. (2019). Decrease  
843 in Seismic Velocity Observed Prior to the 2018 Eruption of Kilauea Volcano  
844 With Ambient Seismic Noise Interferometry. *Geophysical Research Letters*,  
845 *46*(7), 3734–3744. doi: 10.1029/2018GL081609
- 846 Pacheco, C., & Snieder, R. (2005). Time-lapse travel time change of multiply  
847 scattered acoustic waves. *The Journal of the Acoustical Society of America*,  
848 *118*(3), 1300–1310. doi: 10.1121/1.2000827
- 849 Poupinet, G., Ellsworth, W., & Frechet, J. (1984). Monitoring velocity variations  
850 in the crust using earthquake doublets: An application to the calaveras fault,  
851 california. *Journal of Geophysical Research: Solid Earth*, *89*(B7), 5719–5731.
- 852 Rivet, D., Brenguier, F., & Cappa, F. (2015). Improved detection of preruptive  
853 seismic velocity drops at the Piton de La Fournaise volcano. *Geophysical Re-*  
854 *search Letters*, 1–8. doi: 10.1002/2015GL064835.Received
- 855 Rivet, D., Campillo, M., Shapiro, N. M., Cruz-Atienza, V., Radiguet, M., Cotte, N.,  
856 & Kostoglodov, V. (2011). Seismic evidence of nonlinear crustal deformation  
857 during a large slow slip event in Mexico. *Geophysical Research Letters*, *38*(8),  
858 3–7. doi: 10.1029/2011GL047151
- 859 Sandanbata, O., Obara, K., Maeda, T., Takagi, R., & Satake, K. (2015). Sudden  
860 changes in the amplitude-frequency distribution of long-period tremors at Aso  
861 volcano, southwest Japan. *Geophysical Research Letters*, *42*(23), 10256–10262.  
862 doi: 10.1002/2015GL066443
- 863 Segall, P., & Matthews, M. (1997). Time dependent inversion of geodetic data.  
864 *Journal of Geophysical Research: Solid Earth*, *102*(B10), 22391–22409. doi: 10  
865 .1029/97JB01795
- 866 Sens-Schönfelder, C., & Eulenfeld, T. (2019). Probing the in situ Elastic Nonlin-  
867 earity of Rocks with Earth Tides and Seismic Noise. *Phys. Rev. Lett.*, *122*(13),  
868 138501. doi: 10.1103/PhysRevLett.122.138501
- 869 Sens-Schönfelder, C., Pomponi, E., & Peltier, A. (2014). Dynamics of Piton de  
870 la Fournaise volcano observed by passive image interferometry with multiple  
871 references. *Journal of Volcanology and Geothermal Research*, *276*, 32–45. doi:  
872 10.1016/j.jvolgeores.2014.02.012

- 873 Sens-Schönfelder, C., & Wegler, U. (2006). Passive image interferometry and sea-  
874 sonal variations of seismic velocities at Merapi Volcano, Indonesia. *Geophysical*  
875 *Research Letters*, *33*(21), 1–5. doi: 10.1029/2006GL027797
- 876 Shapiro, S. A. (2003). Elastic piezosensitivity of porous and fractured rocks. *Geo-*  
877 *physics*, *68*(2), 482–486. doi: 10.1190/1.1567215
- 878 Snieder, R., Sens-Schönfelder, C., & Wu, R. (2017). The time dependence of rock  
879 healing as a universal relaxation process, a tutorial. *Geophysical Journal Inter-*  
880 *national*, *208*(1), 1–9. doi: 10.1093/gji/ggw377
- 881 Suzuki, Y., Yasuda, A., Hokanishi, N., Kaneko, T., Nakada, S., & Fujii, T. (2013).  
882 Syneruptive deep magma transfer and shallow magma remobilization during  
883 the 2011 eruption of Shinmoe-dake, Japan—Constraints from melt inclusions  
884 and phase equilibria experiments. *Journal of Volcanology and Geothermal*  
885 *Research*, *257*, 184–204. doi: 10.1016/j.jvolgeores.2013.03.017
- 886 Takano, T., Nishimura, T., & Nakahara, H. (2017). Seismic velocity changes concen-  
887 trated at the shallow structure as inferred from correlation analyses of ambient  
888 noise during volcano deformation at Izu-Oshima, Japan. *Journal of Geophysi-*  
889 *cal Research: Solid Earth*, *122*(8), 6721–6736. doi: 10.1002/2017JB014340
- 890 Takano, T., Nishimura, T., Nakahara, H., Ohta, Y., & Tanaka, S. (2014). Seismic  
891 velocity changes caused by the Earth tide: Ambient noise correlation analyses  
892 of small-array data. *Geophysical Research Letters*, *41*(17), 6131–6136. doi:  
893 10.1002/2014GL060690
- 894 Takano, T., Nishimura, T., Nakahara, H., Ueda, H., & Fujita, E. (2019). Sen-  
895 sitivity of Seismic Velocity Changes to the Tidal Strain at Different Lapse  
896 Times: Data Analyses of a Small Seismic Array at Izu-Oshima Volcano.  
897 *Journal of Geophysical Research: Solid Earth*, *124*(3), 3011–3023. doi:  
898 10.1029/2018JB016235
- 899 Takeo, M., Maehara, Y., Ichihara, M., Ohminato, T., Kamata, R., & Oikawa, J.  
900 (2013). Ground deformation cycles in a magma-effusive stage, and sub-Plinian  
901 and Vulcanian eruptions at Kirishima volcanoes, Japan. *Journal of Geophysical*  
902 *Research: Solid Earth*, *118*(9), 4758–4773. doi: 10.1002/jgrb.50278
- 903 Takeuchi, H., & Saito, M. (1972). Seismology: Surface Waves and Free Oscilla-  
904 tions. In B. A. Bolt (Ed.), *Methods in computational physics* (Vol. 11, pp. 217–  
905 295). Academic Press, New York.

- 906 Talwani, P., Chen, L., & Gahalaut, K. (2007). Seismogenic permeability, ks. *Journal*  
 907 *of Geophysical Research: Solid Earth*, *112*(B7).
- 908 Tarantola, A., & Valette, B. (1982). Generalized nonlinear inverse problems solved  
 909 using the least squares criterion. *Reviews of Geophysics*, *20*(2), 219. doi: 10  
 910 .1029/RG020i002p00219
- 911 Tomatsu, T., Kumagai, H., & Dawson, P. B. (2001). Tomographic inversion  
 912 of P-wave velocity and Q structures beneath the Kirishima volcanic com-  
 913 plex, Southern Japan, based on finite difference calculations of complex  
 914 traveltimes. *Geophysical Journal International*, *146*(3), 781–794. doi:  
 915 10.1046/j.1365-246X.2001.00491.x
- 916 Tsukamoto, K., Aizawa, K., Chiba, K., Kanda, W., Uyeshima, M., Koyama, T., ...  
 917 Kishita, T. (2018). Three-Dimensional Resistivity Structure of Iwo-Yama Vol-  
 918 cano, Kirishima Volcanic Complex, Japan: Relationship to Shallow Seismicity,  
 919 Surface Uplift, and a Small Phreatic Eruption. *Geophysical Research Letters*,  
 920 *45*(23), 12,821–12,828. doi: 10.1029/2018GL080202
- 921 Ueda, H., Kozono, T., Fujita, E., Kohno, Y., Nagai, M., Miyagi, Y., & Tanada, T.  
 922 (2013). Crustal deformation associated with the 2011 Shinmoe-dake eruption  
 923 as observed by tiltmeters and GPS. *Earth, Planets and Space*, *65*(6), 517–525.  
 924 doi: 10.5047/eps.2013.03.001
- 925 Van Der Walt, S., Colbert, S. C., & Varoquaux, G. (2011). The numpy array: a  
 926 structure for efficient numerical computation. *Computing in Science & Engi-  
 927 neering*, *13*(2), 22–30.
- 928 Virtanen, P., Gommers, R., Oliphant, T. E., Haberland, M., Reddy, T., Courn-  
 929 peau, D., ... Contributors, S. . . (2019). SciPy 1.0–Fundamental Algorithms  
 930 for Scientific Computing in Python. *arXiv e-prints*, arXiv:1907.10121.
- 931 Wang, Q.-Y., Brenguier, F., Campillo, M., Lecointre, A., Takeda, T., & Aoki,  
 932 Y. (2017). Seasonal crustal seismic velocity changes throughout Japan.  
 933 *Journal of Geophysical Research: Solid Earth*, *122*(10), 7987–8002. doi:  
 934 10.1002/2017JB014307
- 935 Wang, Q. Y., Campillo, M., Brenguier, F., Lecointre, A., Takeda, T., & Hashima, A.  
 936 (2019). Evidence of Changes of Seismic Properties in the Entire Crust Beneath  
 937 Japan After the Mw 9.0, 2011 Tohoku-oki Earthquake. *Journal of Geophysical*  
 938 *Research: Solid Earth*, *124*(8), 8924–8941. doi: 10.1029/2019JB017803

- 939 Weaver, R., Froment, B., & Campillo, M. (2009). On the correlation of non-  
 940 isotropically distributed ballistic scalar diffuse waves. *The Journal of the*  
 941 *Acoustical Society of America*, *126*(4), 1817–26. doi: 10.1121/1.3203359
- 942 Weaver, R., Hadziioannou, C., Larose, E., & Campillo, M. (2011). On the precision  
 943 of noise correlation interferometry. *Geophysical Journal International*, *185*(3),  
 944 1384–1392. doi: 10.1111/j.1365-246X.2011.05015.x
- 945 Weaver, R., & Lobkis, O. (2000). Temperature dependence of diffuse field phase. *Ul-*  
 946 *trasonics*, *38*(1), 491–494. doi: 10.1016/S0041-624X(99)00047-5
- 947 Wegler, U., Nakahara, H., Sens-Schönfelder, C., Korn, M., & Shiomi, K. (2009).  
 948 Sudden drop of seismic velocity after the 2004 Mw 6.6 mid-Niigata earthquake,  
 949 Japan, observed with Passive Image Interferometry B06305. *Journal of Geo-*  
 950 *physical Research: Solid Earth*, *114*(6), 1–11. doi: 10.1029/2008JB005869
- 951 Wegler, U., & Sens-Schönfelder, C. (2007). Fault zone monitoring with passive image  
 952 interferometry. *Geophysical Journal International*, *168*(3), 1029–1033.
- 953 Wessel, P., Smith, W. H. F., Scharroo, R., Luis, J., & Wobbe, F. (2013). Generic  
 954 mapping tools: Improved version released. *Eos, Transactions American Geo-*  
 955 *physical Union*, *94*(45), 409-410. doi: 10.1002/2013EO450001
- 956 Yamada, T., Ueda, H., Mori, T., & Tanada, T. (2019). Tracing Volcanic Activ-  
 957 ity Chronology from a Multiparameter Dataset at Shinmoedake Volcano  
 958 (Kirishima), Japan. *Journal of Disaster Research*, *14*(5), 687–700. doi:  
 959 10.20965/jdr.2019.p0687
- 960 Yamamura, K., Sano, O., Utada, H., Takei, Y., Nakao, S., & Fukao, Y. (2003).  
 961 Long-term observation of in situ seismic velocity and attenuation. *Jour-*  
 962 *nal of Geophysical Research: Solid Earth*, *108*(B6), 1–15. doi: 10.1029/  
 963 2002JB002005
- 964 Zhu, C., Byrd, R. H., Lu, P., & Nocedal, J. (1994). Fortran subroutines for large-  
 965 scale bound constrained optimization. *ACM Trans Math Softw*, *23*(4), 550–  
 966 60.

## 967 **Appendix A Calculation of the likelihood**

968 For an efficient evaluation of the likelihood defined by equation (32), calculation  
 969 of the determinant of a large matrix  $\mathbf{F}_t$  ( $N \times N$  matrix) becomes the bottleneck. To re-  
 970 duce the calculations, we rewrote the definition of the likelihood as follows. Since  $\mathbf{Z}_t \hat{\mathbf{P}}_{t|t-1} \mathbf{Z}_t^T$

971 is the symmetric matrix, it can be diagonalized by the unitary matrix  $\mathbf{U}$  as

$$972 \quad \mathbf{U}^t \mathbf{F}_t \mathbf{U} = \mathbf{\Lambda}, \quad (\text{A1})$$

973 where the eigen matrix  $\mathbf{\Lambda}$  can be written

$$974 \quad \mathbf{\Lambda} \equiv \begin{pmatrix} \lambda_1 & 0 & 0 & \cdots & 0 \\ 0 & \lambda_2 & 0 & \cdots & 0 \\ 0 & 0 & 0 & \cdots & 0 \\ \vdots & \vdots & \vdots & \ddots & 0 \\ 0 & 0 & 0 & \cdots & 0 \end{pmatrix}, \quad (\text{A2})$$

975 Since the rank of  $\mathbf{Z}_t \hat{\mathbf{P}}_{t|t-1} \mathbf{Z}_t^T$  is 2, the other  $N - 2$  eigen values are zeros.

976 Then the determinant can be written by

$$977 \quad \det(\mathbf{F}_t) = \det(\mathbf{U}^T \mathbf{F}_t \mathbf{U}) = \det(\mathbf{\Lambda} + h_0 \mathbf{I}) = (\lambda_1 + h_0)(\lambda_2 + h_0)h_0^{N-2}. \quad (\text{A3})$$

978 Here we consider the eigen values of  $\mathbf{Z}_t \hat{\mathbf{P}}_{t|t-1} \mathbf{Z}_t^T$ . For a given eigen vector  $\mathbf{x}_i$  for eigen  
979 value  $\lambda_i$ ,

$$980 \quad \mathbf{Z}_t \hat{\mathbf{P}}_{t|t-1} \mathbf{Z}_t^T \mathbf{x} = \lambda_i \mathbf{x}_i. \quad (\text{A4})$$

981 Multiply both sides of each equation by  $\mathbf{Z}_t$

$$982 \quad \mathbf{Z}_t^T \mathbf{Z}_t \hat{\mathbf{P}}_{t|t-1} \mathbf{Z}_t^T \mathbf{x} = \lambda_i \mathbf{Z}_t^T \mathbf{x}_i. \quad (\text{A5})$$

983 Since this equation can be interpreted as an eigen value problem for the smaller matrix

984  $\mathbf{Z}_t^T \mathbf{Z}_t \hat{\mathbf{P}}_{t|t-1}$  ( $2 \times 2$  matrix), we can obtain these efficiently.